DESIGN, CONTROL, AND HUMAN SUBJECT EVALUATION OF POWERED HIP EXOSKELETONS

A Dissertation
Presented to
The Academic Faculty

by

Hsiang Hsu

In Partial Fulfillment
of the Requirements for the Degree
Master of Science in the
School of Mechanical Engineering

Georgia Institute of Technology
May 2019

DESIGN, CONTROL, AND HUMAN SUBJECT EVALUATION OF POWERED HIP EXOSKELETONS

Approved by:

Dr. Aaron J. Young Advisor
School of Mechanical Engineering
Georgia Institute of Technology

Dr. Gregory Sawicki
School of Mechanical Engineering
Georgia Institute of Technology

Dr. Anirban Mazumdar
School of Mechanical Engineering
Georgia Institute of Technology

Date Approved: [04 22, 2019]

ACKNOWLEDGEMENTS

This work is a collection of the studies and research I have conducted during my time pursing my master's degree in Mechanical Engineering at Georgia Tech. It is with the support and guidance from those around me that I am able to present this work. First, I would like to send a special thanks to Dr. Aaron Young for supporting my research work and providing guidance when needed.

I would also like to thank Inseung Kang, who has been a mentor to me in EPIC lab. In addition, I would like the acknowledge and thank my peers and undergraduate students in EPIC lab who I had a chance to collaborate with. I would like to thank Dr. Sawicki and Dr. Mazumdar for serving on the committee for my thesis. I am also thankful for the various faculties and staffs of Georgia Institute of Technology who taught me valuable lessons.

Finally, I would like to acknowledge with gratitude, the support and love from my family and close friends, especially my parents, who have always been a great support throughout my life. Special thanks to my girlfriend, Christie Choi, for providing both physical and moral support during this entire process. Thank you all who have helped through this journey that I may have not mentioned above.

TABLE OF CONTENTS

LIST OF FIGURES

LIST OF SYMBOLS AND ABBREVIATIONS

EMG	Electromyography
FSR	Force Sensitive Resistor
SEA	Series Elastic Actuator
BLDC	Brushless DC
GM	Gluteus Maximus
RF	Rectus Femoris
PRF	Proximal Rectus Femoris
GMed	Gluteus Medius
BF	Biceps Femoris
VL	Vastus Lateralis
AM	Adductor Magnus
DBF	Distal Biceps Femoris
RMS	Root Mean Square
SVM	Support Vector Machine
NN	Neural Networks
LDA	Linear Discriminant Analysis
MAV	Mean Absolute Value
ZC	Zero Crossing
SSC	Slope Sign Change
WL	Waveform Length

SUMMARY

Powered lower-limb exoskeletons have potentials to revolutionize many fields such as industrial, military, and clinical industries. Most lower-limb exoskeletons are complex multi-joint devices that are often limited by their weight, convoluted controllers, and imperfect power transmissions. To make exoskeletons more robust, researchers are re-focusing on single-joint devices and studying the effects of human-machine interaction. While both the ankle joint and hip joint are main torque contributors during level walking, the hip joint is less efficient due to the lack of spring-like tendons. As a result, providing hip joint assistance may be more impactful than aiding other joints.

This thesis proposes a top-down approach towards wearable robotics by designing, building, and testing two versions of torque-controllable exoskeletons. The goal is to understand how to achieve the best performance through novel designs and controllers. Hip Exo v1.0 and Hip Exo v2.0 both utilize series elastic actuator design to achieve closed-loop torque control. Hip Exo v1.0 is validated through an assistance magnitude study and a proportional EMG profile pilot. Hip Exo v2.0 is developed to fix many of the design flaws from Hip Exo v1.0 through new mechanical and electrical designs. The improved Hip Exo v2.0 allows for the development and implementation of next-generation EMG pattern recognition controller. An EMG delay pilot, EMG pattern recognition pilot, and speed/ramp estimator pilot are performed with Hip Exo 2.0. All the human subject studies give valuable insights into understanding how human interacts with wearable robots. The findings of this thesis act as a comprehensive guide for design, control, and human subject validation of powered hip exoskeletons.

CHAPTER 1. INTRODUCTION

An exoskeleton, a wearable suit that modifies human performance, has existed since the late 19th century [1]. However, exoskeleton technology has only recently made significant strides in progress due to breakthroughs in battery and computing technologies. Most of the commercially available exoskeletons are used in three environments: industrial, military, and medical [2]. Construction and automobile companies use exoskeletons to enhance productivity and prevent injuries from muscle exhaustion [3]. The U.S. military develops performance-augmenting exoskeletons to help soldiers carry heavy loads over long distances [4]. Healthcare professionals employ exoskeletons as rehabilitation devices to help injured patients learn how to walk again [5]. Exoskeletons can be categorized as upper-limb, lower-limb, or full-body exoskeletons (Fig. 1). They can also be further classified by their power source and transmission as powered/passive and rigid/soft exoskeletons. This thesis is specifically focused on the works contributed to the rigid powered hip exoskeleton field.

Existing commercial exoskeletons, such as Indego [6], Rewalk [7], and EksoGT [8], often feature multiple actuators at different joints. The added weights and degrees of freedom (DOF) often make designing hardware and software significantly more challenging. The engineering complexity grows exponentially as active components are added. As a result, exoskeleton technology has only shown limited success for very specific applications [9]. While these devices may benefit targeted users, the general human-machine interactions still remain largely unclear and understudied. To overcome such limitations, many research and industry groups are developing single-joint exoskeletons

[10-14]. Due to their simpler nature, single-joint exoskeletons can be applied to different populations. In fact, many of those devices have achieved significant metabolic benefits due to their more optimized designs and intelligent controllers [10, 12, 13].

Figure 1. Three types of commercially available powered exoskeletons used in different applications. (Left) Industrial Full-Body Powered Exoskeleton for human augmentation by Sacros Robotics [15]. (Middle) Medical Lower-Limb Exoskeleton for rehabilitation by Ekso Bionics [16]. (Right) Single-joint Hip Exoskeleton for mobility assistance by Honda [17].

Biomechanically, the ankle joint provides high positive mechanical work during walking. As a result, many exoskeletons often target the ankle joint and have achieved better metabolic performances [12, 18]. Despite also being a main mechanical power contributor (45%), the hip joint is estimated to be 2 times less efficient than the ankle joint due to lack of one or more spring-like elements (e.g. Achilles tendon unit) [19]. Recent studies demonstrate that by targeting the hip joint, exoskeletons can improve the metabolic

cost more efficiently with less assistance [13]. In addition, powered hip exoskeleton could potentially provide a solution to stroke and elderly populations who clinically rely on their hip to ambulate. While early preliminary results show great promises, the limited number of the hip exoskeleton studies leave many research questions unanswered [20-22]. The main goal of this thesis is to attempt to address the ultimate question of how to design an effective powered hip exoskeleton. The Hip Exo v1.0 is first developed, programmed, and human subject validated (Fig. 2). Then, many key findings are used to create the augmented Hip Exo v2.0 with better performance and capabilities.

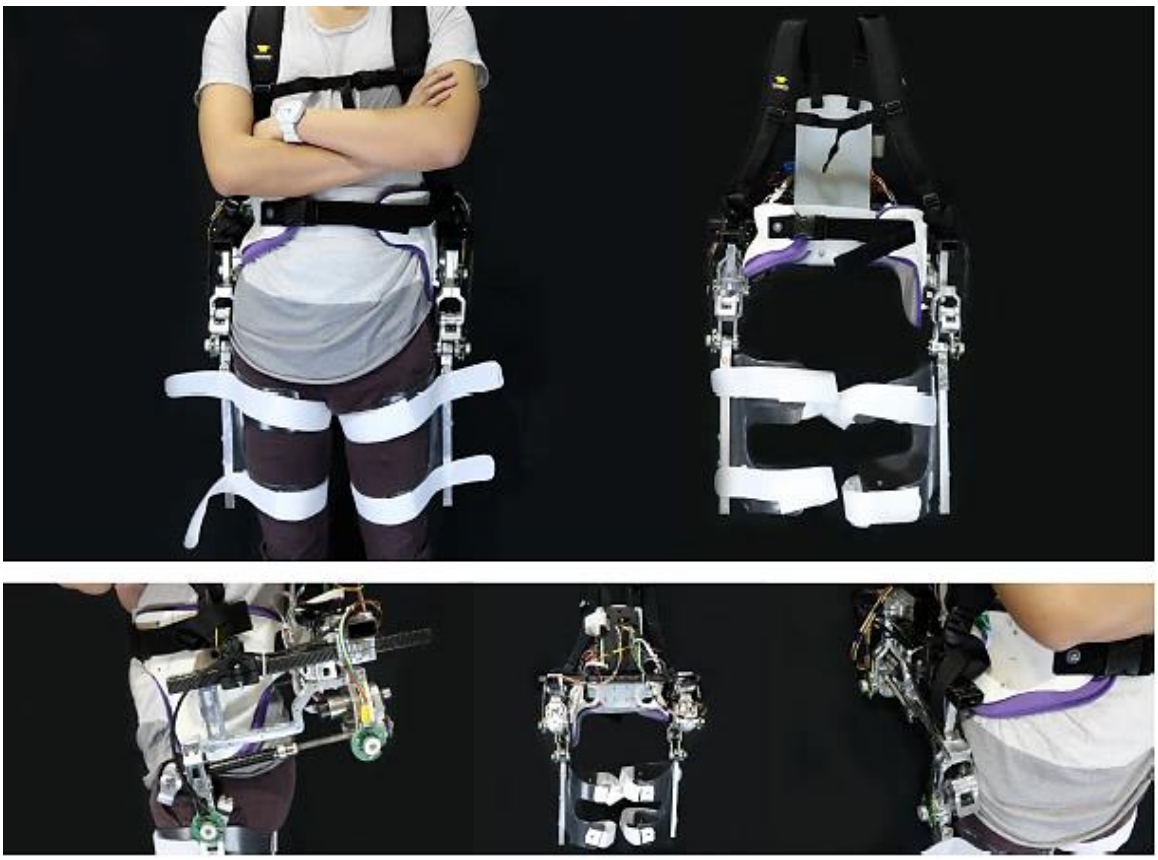

Figure 2. The first-generation powered hip exoskeleton developed at the Georgia Institute of Technology's EPIC Lab. The Hip Exo v1.0 is designed to be a flexible platform where different sensors and equipment can be used to conduct novel research initiatives. The goal of the project is to further understand human machine interactions and contribute to future designs and studies for wearable robots.

The thesis is divided into three main sections: (1) device design and development, (2) intelligent controller formulation and deployment, and (3) human subject testing and validation. In the first section, two novel ball-screw driven bilateral hip exoskeletons designs are introduced. The devices are equipped with series elastic actuators (SEA) for controllable torque assistance in hip flexion and extension directions. In addition, custom PCB designs and electronics architectures are documented to provide the foundation for the intelligent controllers. Hip Exo v1.0's human subject testing provides valuable insights into how to physically engineer a robust and effective hip exoskeleton according to human biomechanics. In the second section, three different control strategies are presented: biological torque controller, proportional electromyography (EMG) controller, and a unique EMG pattern recognition controller. Onset timing, magnitude, and duration are the three key parameters any controllers use to generate their assistance profiles. The biological torque controller uses mechanical sensors for inputs, whereas the two EMG controllers uses the user's muscle signals. The controllers differ in how they obtain the key parameters for assistance and these differences allow for unique studies proposed in the next section. The third section presents several human subject tests performed with the exoskeletons. A magnitude study shows how assistance magnitude could impact metabolic performance with the biological torque controller. Two EMG pilots studied demonstrate the feasibility of altering magnitude and onset timing parameters for the EMG controllers. Lastly, two offline EMG-based machine learning studies show how EMG signals are valuable for next-generation wearables. The author aims to present the engineering challenges and important findings from an interdisciplinary and holistic perspective, which is not as readily available in the current powered hip exoskeleton literatures.

CHAPTER 2. HIP EXOSKELETON DEVICE DESIGN

The two proposed hip exoskeletons are designed to provide external mechanical torque at hip joint during walking (Fig. 3). Therefore, the active power assistance is in the hip flexion and extension directions. Passive joints are added for free hip abduction and adduction in the frontal plane. The exoskeletons compose of three main parts: the actuator and sensor unit, the backpack unit, and the orthosis/interface unit. Both hip exoskeletons use SEA units for their closed-loop torque control. SEA concept has been introduced in several robotic applications due to its robustness in measuring the output torque while maintaining a simple overall form factor [11, 14, 23]. Additionally, both exoskeletons opt for low-friction ball-screw transmissions to achieve back-drivability, which allows the user to move freely in case of emergency power off situations.

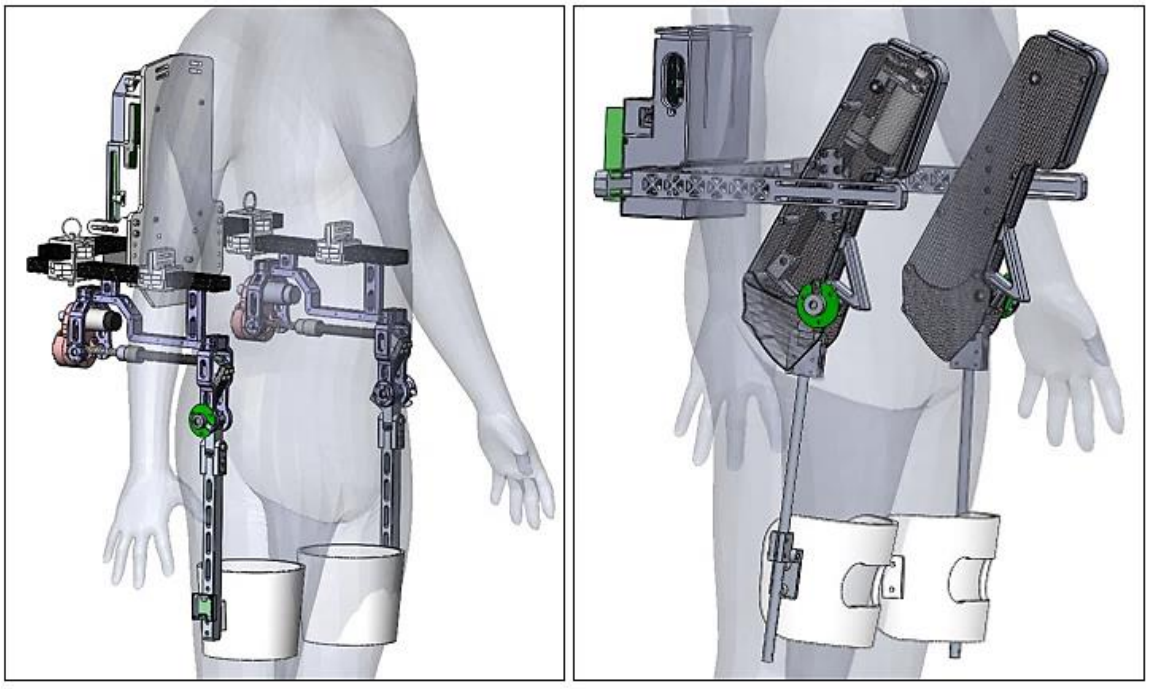

Figure 3. Two developed powered hip exoskeletons. Both devices use SEA designs to perform closed-loop torque control. The v1.0 is not only significantly larger and heavier than the v2.0, but also lacks many features such as sensor protection, signal conditioning, and modularity. (Left) Hip Exo v1.0 (Right) Hip Exo v2.0.

Hip Exo v1.0, is designed to match up to 100% of the root-mean-square biological torque of a 70kg adult walking at 1.0 m/s [24]. It has a continuous torque of 30 Nm and a maximum angular velocity of 180°/s. The active joint has a 50° to -20° range of motion for flexion and extension. The passive joint has a 15° to -15° range of motion for abduction and adduction. Hip Exo v1.0 uses an off-the-shelf orthosis pelvis band and custom-made thigh cuffs with the entire device weighing about 7.8 kg. The main limitation of Hip Exo v.1.0 is speed and torque trade-off. Significant delayed is observed during the human subject testing, which influences the designed specification of Hip Exo v2.0. The study shows that an optimal assistance exists around smaller torque range (15 ~ 20 Nm), which suggests that a lower torque but higher speed device may be more appropriate.

The second iteration of the hip exoskeleton, Hip Exo v2.0, is built entirely separate to improve on the various design flaws of its predecessor. The exoskeleton is augmented for a 70kg adult walking at 1.4 m/s. The new device has a continuous torque of 20 Nm and a maximum angular velocity of 300°/s. The sagittal range of motion is now 100° to -20° and allows the user to sit down while wearing the exoskeleton. The passive joint is slightly reduced (10° to -10°) in exchange for protective covers. The new exoskeleton utilizes new modular orthosis and thigh cuff designs for greater adjustability. The device weights about 6.8 kg. More importantly, Hip Exo v2.0 can now interface with different external clinical systems, which is crucial for more advance controller and complex experimental protocols.

2.1 Hip Exoskeleton v1.0 Design

2.1.1 System Architecture (v1.0)

Each actuator and sensor unit is composed of a 200W brushless DC motor (EC30, Maxon Motor, Switzerland), a set of 2:1 aluminium timing belt pulleys (Misumi, USA), a 10 mm ball screw (Thomson Linear Motion, USA), a modified fiberglass spring (Gordon

Composites, USA), four sets of strain gauges (Omega Engineering, USA), a force-sensitive resistor (FSR), an absolute magnetic encoder (Orbis, Renishaw, UK), and two inertial measurement units (Micro USB, Yost Labs, USA). The actuator unit is designed to be a SEA, where the spring deflection can be used to control the exoskeleton torque output. The fiberglass spring deflection is measured through four strain gauges and feeds to the microprocessor for closed-loop torque control. Two-stage signal amplification and conditioning are required since the raw strain gauge signal is microscopic (~1 mV). Other external sensors, such as hip joint encoder and force-sensitive resistor readings, are sent to the microprocessor through a mixed-signal PCB. The microprocessor housed in the backpack unit computes the appropriate high-, mid-, and low-level commands based on the available sensor information received (Fig. 4).

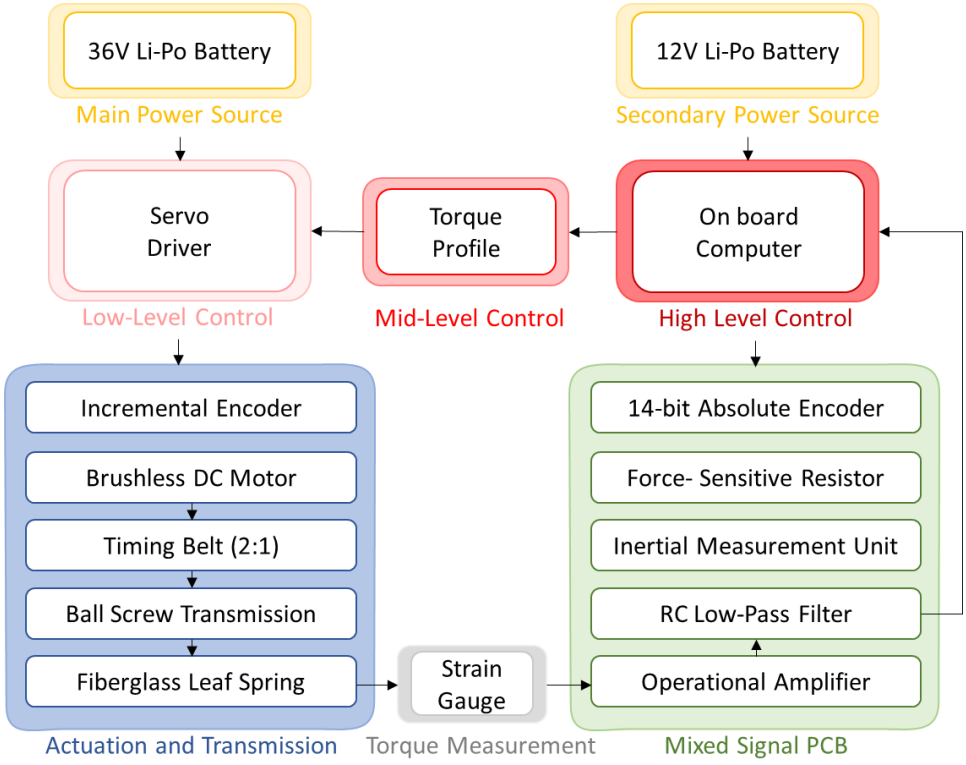

Figure 4. Hip Exo v1.0 system architecture. The 36V battery powers the entire actuator units. The microprocessor (myRIO) is powered by a separate 12V battery and communicates with the sensors through the mixed-signal PCB board. The microprocessor also hosts the three control layers: high, mid, low-level controller.

The backpack unit houses a custom PCB, a single board computer (myRIO, National Instruments, USA), two servo drivers (ESCON 50/5 Module, Maxon Motor, Switzerland), and two 18.5 V Li-Po batteries (Venom Power, USA). The Maxon motors are equipped with internal hall-effect sensors and incremental encoders for motor-level control. All other external sensors, such as the absolute encoders, force-sensitive resistors, and strain gauges, are joined by the custom mixed-signal PCB (Fig. 4).

The interface unit is made up of three parts: custom made thigh shells, an orthotic pelvic band (Newport 3, Orthomerica, USA), and a set of shoulder straps. A carbon fiber C-frame is used to secure the actuator units to the orthosis band by a three-point attachment system. Two thigh shells are custom molded with carbon infused polycarbonate material for strength. Since most of the interface unit is not adequately adjustable, many subjects experience sub-optimal fittings and poorer power transmissions from the exoskeleton.

2.1.2 Mechatronics Design (v1.0)

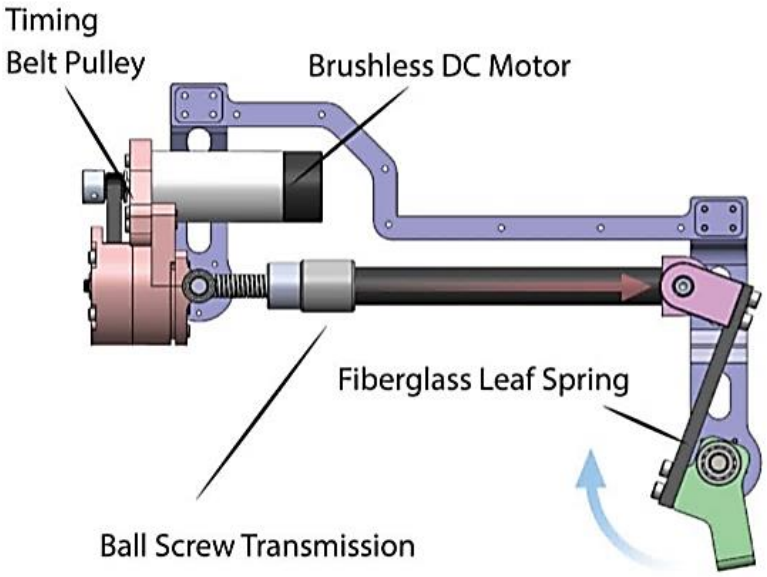

Figure 5. Actuator unit of the Hip Exo v1.0. The BLDC motor torque is amplified through the timing belt the ball-screw transmission. The linear force is translated to torque on the fiberglass spring through pivoting hip joint.

The SEA design consists of a timing belt pulley, ball-screw driver coupled with a carbon fiber tube, and a fiberglass spring (Fig. 5). Fiberglass springs offer excellent power density compared to traditional metals such as steel or titanium [25, 26]. However, they require extreme care and special machines (5-axis OMAX waterjet, USA) to prototype due to the harmful by-product dust. The exoskeleton torque (τ_{hip}) is governed by Eq. 1 where N is the timing belt pulley ratio, R is the fiberglass spring moment arm, P is the pitch of the ball screw, α is the spring orientation, and τ_{motor} is the BLDC motor torque. Detailed calculation of the α angle is included in the Appendix. To account for friction losses, a low-level PD controller ensures that the commanded hip torque (Eq. 1) matches the output torque measured by the strain gauges. A comprehensive explanation of the low-level controller is explained in the next chapter.

$$\tau_{hip} = \frac{2\pi NR\cos\alpha}{P}\tau_{motor} \tag{1}$$

The initial design attempts to use two rotary encoders and a geometrical model to compute the deflection of the spring. However, the resulting torque resolution is severely limited by the 14-bit encoders. The poor torque reading becomes problematic when it was used in the low-level PD feedback, where slight error would cause the derivative term to approach infinity. Consequently, a direct measurement of spring deflection was more appropriate by using a full-wheat stone bridge to achieve much finer torque readings.

While it may be more complex to implement, the full-wheat stone bridge setup allows for drift compensations compared to a quarter or half-bridge. The fiberglass spring behaves like a fixed cantilever beam and a special full-wheat stone bridge alignment is installed to maximize bending sensitivity (Fig. 6). Each of the 350 Ω strain gauges are placed in a way where a pair of voltage dividers are always experiencing opposite strains. Between the two voltage dividers, wirings are convoluted so the voltage changes happen

in opposite directions to maximize the resolution. The strain gauge output signals are wired to a custom PCB and amplified through a general-purpose operational amplifier (AD623, Analog Devices, USA). In order to convert a differential signal into a single-ended signal, a +2.5V offset is added to the amplified strain gauge reading for microprocessor sampling (0 – 5V). Furthermore, the output signal is passed through a passive first-order RC low-pass filter (10 Hz). Each spring is manually calibrated against a set of known weights. A linear approximation function, which converts analog voltage to applied force, can be generated. The linear regression function is used in conjunction with Eq. 1 and the PD controller to calculate the corrected command for the motor.

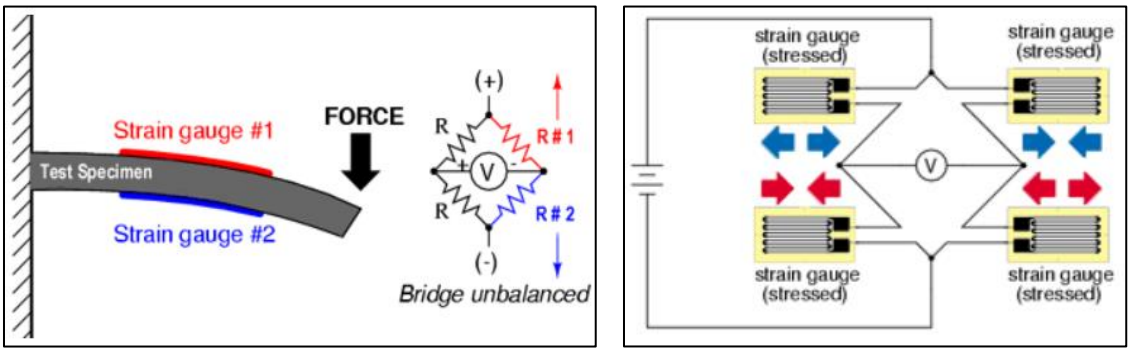

Figure 6. Wheat stone bridge setups for bending applications [27]. (Left) For each voltage divider, the strain gauges are placed in a way where one would experience tension while the other would experience compression. (Right) Left and right voltage dividers are set in opposite side of the beam so maximum differential voltage will be achieved under loading.

2.1.3 Benchtop Validation (v1.0)

The PD controller is empirically tuned with a maximum of 20 Nm in both flexion and extension directions. Three different step inputs (5 Nm, 10 Nm, and 15 Nm) are applied with a pre-load of 2 Nm to ensure the ball-screw backlash is compensated during benchtop characterization (Figure 7). Due to the low derivative term, the smaller step-inputs have fairly damped responses, while higher inputs have increased initial overshoots and settling

times. The highest overshoot is about 15% for 15Nm input. The settling time of the step response is approximately 0.6 s, 0.9 s. and 1.1 s for the 3 different torque inputs.

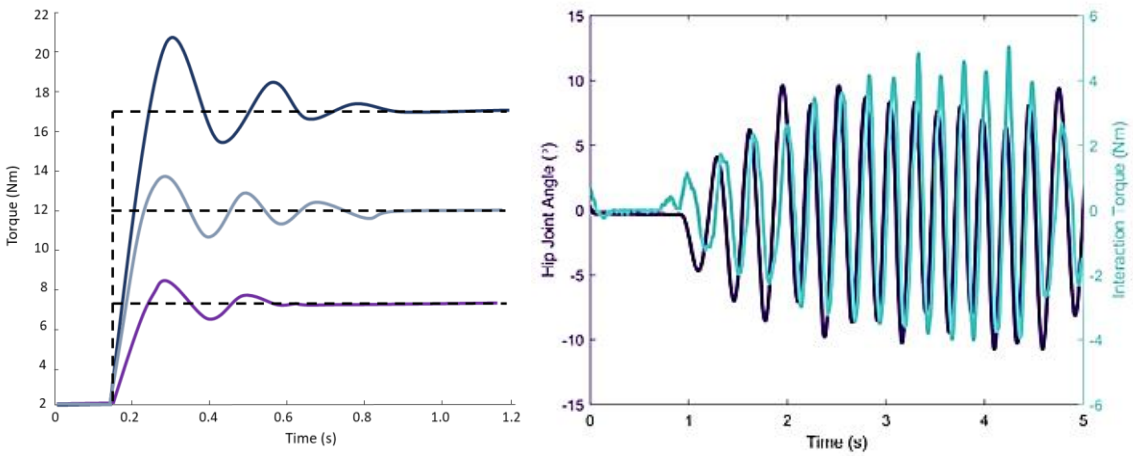

Figure 7. Step-input and Sinusodial-input for Hip Exo v1.0 benchtop characterization. (Left) Three step responses are recorded to provide insights into time domain. (Right) 2Hz sine wave responses show how the device respond to walking emulation of around 1.6 m/s.

The frequency response of the device is tested by emulating the user walking in a zero-impedance mode (Fig. 7). Zero-impedance mode is a control mode where the desired torque command is set to zero. By doing so, the actuator actively cancels out the residual torque and allows the exoskeleton to actively follow the user's leg movement. A 2Hz sine wave is manually generated with a 20° range of motion in both directions to emulate walking speed of 1.6 m/s [28]. The green line in Fig. 7 represents the residual interaction torque and it increases with the increase in the range of motion. The zero-impedance mode resulted in RMSE of 2.28 Nm. While the device's torque tracking does not achieve perfect "zero" tracking, the performance is somewhat reasonable as the very first prototype. The Hip Exo v2.0 overcomes the torque tracking imperfection through numerous mechanical and electrical modifications.

2.2 Hip Exoskeleton v2.0 Design

2.2.1 System Architecture (v2.0)

After the first exoskeleton is clinically tested with an able-body study (n = 10), several mechanical and electrical design limitations were identified. While the main powered electronics remained the same, Hip Exo v2.0 undergoes various mechanical and electrical design changes, including a new mechanical transmission setup, dedicated PCB boards, and unified power harnesses (Fig. 8). These new designs significantly boost the reliability, efficiency, and modularity of the entire exoskeleton.

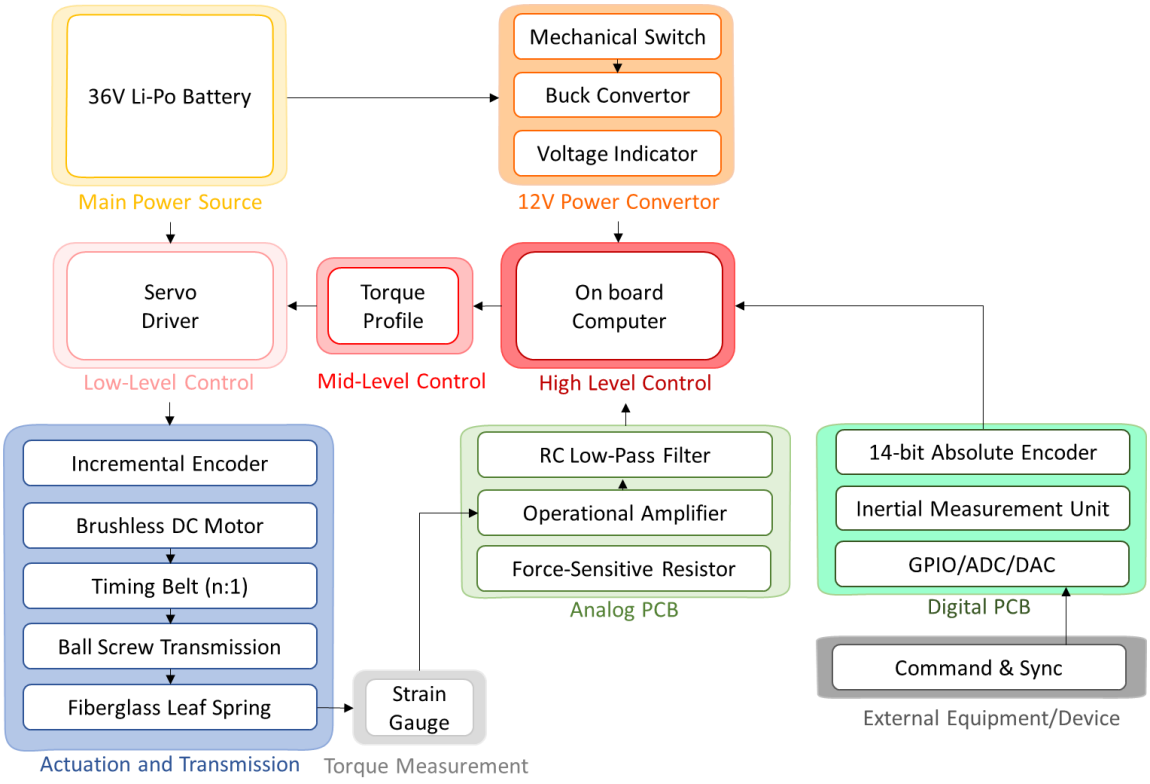

Figure 8. Hip Exo v2.0 System Architecture. An additional 12V step-down convertor is implemented to make better use of the main battery and the regenerated energy. Moreover, the PCB is now separated into dedicated analog board and digital board to ensure signal integrity. Lastly, extended GPIO pins allows other equipment such as EMG sensors or motion capture to easily interface with Hip Exo v2.0.

The Hip Exo v1.0's backpack unit is not designed to house the battery on-board. To achieve over-ground autonomy, the additional battery and the main battery must both be manually secured to the interface. Furthermore, since the returning energy from the motor free-spinning is not being properly utilized, the servo drivers often face an overvoltage issue that forces the entire device to shut-off during a high torque assistance. Lastly, there are no indications when the main battery becomes unstable due to excessive use, which could potentially lead to dangerous situations. The second version of the device underwent an overhaul on the entire power harness for safer and better use of the battery. A DC-to-DC buck convertor is added to power the microprocessor directly from the main battery. This not only eliminates the need for additional battery, but also allows some of the re-generative energy to be recycled. As a result, the servo drivers experience less over-voltage errors. Moreover, an additional LED voltage indicator is added to monitor the power status of the exoskeleton. The updated PCB boards allows Hip Exo v2.0 to interact with external devices and equipment such as EMG sensors or the motion capture systems.

A new 4-part system orthosis unit (Fillaeur, USA) replaces the off-the-shelf pelvic band. The new unit composes of interconnected parts to accommodate various body sizes and shapes. Two side plates, one front plate, and one back plate secure the user's trunk through adjustable buckles for personalized fitting. The additional plates provide a bigger surface area for more even power distribution. The thigh cuff mounting mechanism is also redesigned to interchange various cuff sizes (S, M, L, XL) easily. An aluminium 7075 C-frame with slot mechanism makes fine adjustability in both the sagittal and the frontal plane possible. The C-frame also allows for effortless alignment of the device's output joint without having to detach the actuator unit like the previous iteration. The same 3-point attachment mounting system is preserved to ensure thorough power transmission.

2.2.2 Mechatronics Design (v2.0)

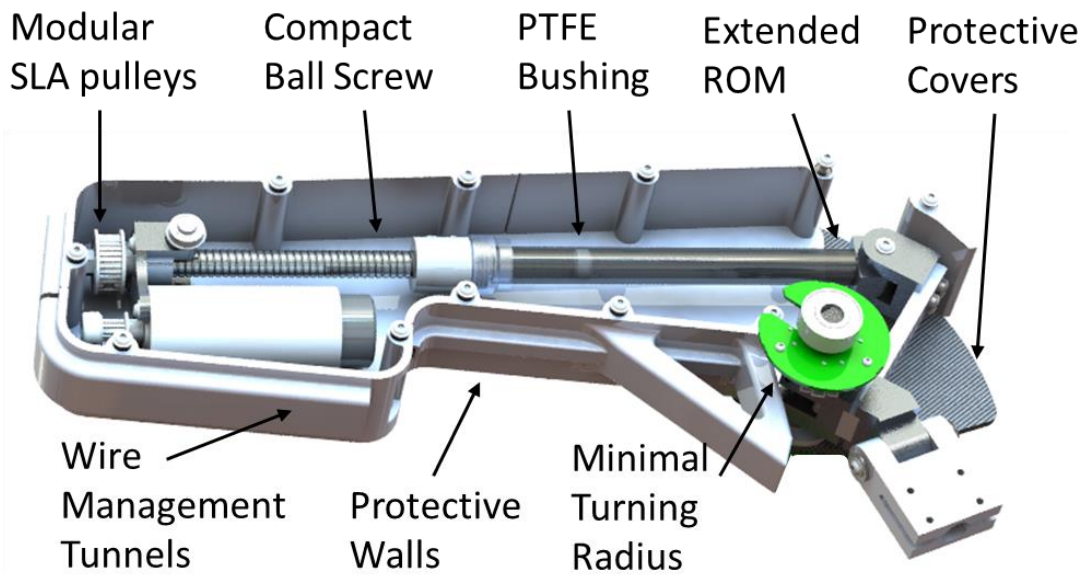

Figure 9. Rotated new actuator unit for Hip Exo v2.0. The PTFE bushing, minimal turning radius, and protective covers enhance the reliability of the device. SLA pulleys, new lead screws, and extended ROM allow the device to be more flexible.

Hip Exo v2.0 is re-designed to be more mechanically secured, reliable, and modular (Fig. 9). During initial human subject testing, the user wearing Hip Exo v1.0 often experienced significant torque delays due to its lower angular velocity. Hip Exo v2.0 is optimized for smaller torque range (20 Nm), but with higher speed capability (220°/s). Utilizing 3D printable resin pulleys (Formlabs, USA), modular gear ratio can be achieved through 3D CAD design modification. A new PTFE linear bushing is added at the tip of the ball screw shaft to ensure proper transmission alignments. The entire actuator unit is reoriented vertically to improve the moment arm efficiency for walking. Hip Exo v2.0 has an average 97.7% efficiency comparing to Hip Exo v1.0's 89.6%. Finally, the main transmission components are encased by 3D printed walls and protective covers. The new housing not only protects the sensitive sensing units but also minimizes vibrations.

Electronically, one major reliability flaw of Hip Exo v1.0 is the addition of the strain gauge sensors towards of the end of the design cycle. Faulty strain gauge reading is catastrophic because it is the most critical component in the closed-loop feedback controller. Since the device is not designed to accommodate the additional strain gauges, the sensors often fail and cause exoskeleton malfunctions. The three main overlooked causes of the failures are incorrect spring thickness, unprotected strain gauges, and extreme bending radius. Even though a finite element analysis is used for spring thickness calculation, the assumption of static loading proves to be problematic. In practice, the user also applies a dynamic force to the spring in conjunction with the motor force. Consequently, the dynamic strains often exceed the strain gauge's breaking limit and provoke sudden failures. Therefore, the safety factor for the spring thickness is doubled to prevent permanent damages to the strain gauges.

In the previous PCB design, all signals are presented on the same board, including the sensitive strain gauge signals. High-speed digital signals like SPI and PWM present serious concerns for signal contamination induced by the fast switching digital signal. For this reason, the new PCB design separates the boards into dedicated analog and digital boards. The fragile analog torque signals are thus less likely to have noise. Thicker spring means less deflection and thus less torque resolution. The trade-off in signal resolution is compensated by implementing a potentiometer for higher and adjustable gain on the operational amplifier. A more aggressive (7 Hz) low-pass RC filter is also placed for better noise rejections. The exposed strain gauges and the considerable wire bending also play a big part in numerous sensor malfunctions. Therefore, a new strain gauge wire tunnel is carefully designed to minimize the bending radius of the wires. The 3D printed wall and

tunnel are designed to have the wires pass through the center of rotation as much as possible to avoid excessive bending. Lastly, all wires are made with new silicon insulation, which are much more resilient to repeated motions compared to regular insulation.

2.2.3 Benchtop Validation (v2.0)

A similar benchmark matrix is performed on the new exoskeleton. Both the step input and sinusoidal responses are better than those of the previous exoskeleton (Fig. 10). The highest overshoot is decreased to 6% for the 15 Nm input. Interaction torque RMSE also decreased to only 0.31 Nm for the 2Hz sinusoidal input. The electro-mechanical upgrades and separated PCBs result in much cleaner and stable strain gauge signals during movement. As a result, much more aggressive PD parameters can be used for Hip Exo v2.0's low-level layer. Throughout all the benchtop testing and walking pilots (~ 4 months), Hip Exo v2.0 has not had any strain gauge or mechanical failures yet. In contrast, the Hip Exo v1.0's strain gauge sensors usually only last 2 – 3 weeks of use.

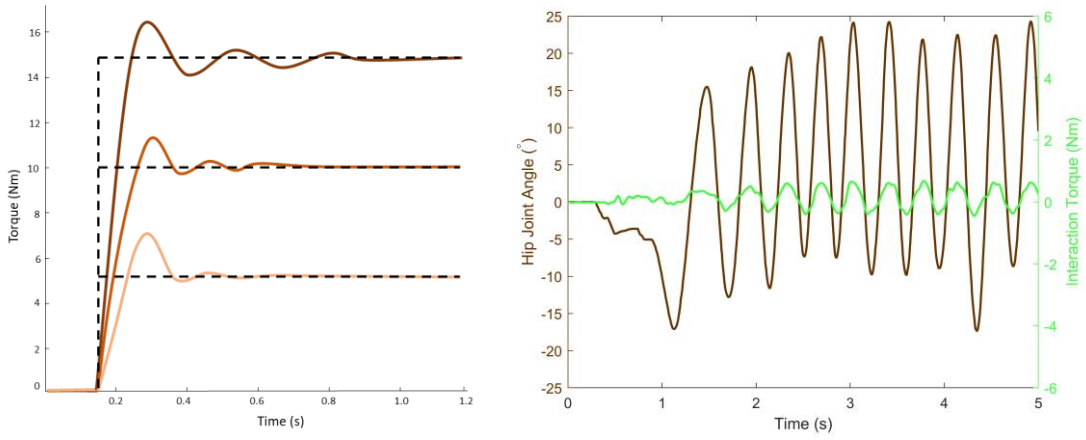

Figure 10. Step-input and Sinusodial-input for Hip Exo v2.0 benchtop characterization. (Left) Three step responses are recorded to provide insights into time domain. (Right) Pseudo-sine wave responses are also recorded to provide insights into frequency domain.

CHAPTER 3. HIP EXOSKELETON CONTROL STRATEGY

This thesis presents three control strategies for the hip exoskeletons: (1) Biological torque controller, (2) proportional EMG controller, and (3) EMG pattern recognition controller. Each presented control strategy consists of three distinct layers: low-level layer, mid-level layer, and high-level layer (Fig. 11). The high-level layer makes general decision about the state of the user. The mid-level layer generates the assistance torque profile according to the user's state information. The low-level layer ensures the applied torque is matched to the desired torque commanded. The hierarchical structure makes the implementation of different control strategies more efficient by modulating the code.

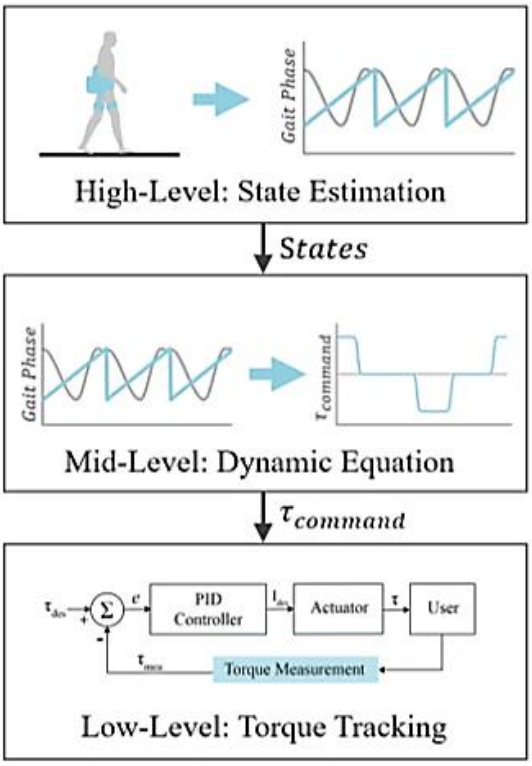

Figure 11. High, Mid, Low-level architecture. The high-level layer estimates the user's state. The mid-level layer generates the appropriate assistance profile. The low-level layer checks the applied torque against the commanded torque.

3.1 High, Mid, and Low-level Layer Overview

3.1.1 High-level Layer

A high-level layer often composes of different state approximation algorithms. Two of the most common lower-limb exoskeleton algorithms are intent recognition and gait phase estimation. The intent recognition system often uses peripheral sensors and machine learning techniques to infer the user's intent, such as walking, sitting, or stair climbing [29]. For the gait phase estimator, many groups simply replace it with a finite state machine by discretizing the gait cycle into different states such as stance and swing [30]. Although easy to implement, a finite state machine often performs poorly due to the discontinuity in between states. For example, the control parameters for stance phase might be completely different from those of the swing phase. Therefore, both hip exoskeletons presented in this thesis implement mostly continuous high-level estimators for smoother outputs.

3.1.2 Mid-level Layer

The mid-level layer primarily consists of various dynamic equations that convert the high-level layer decision in to exoskeleton outputs. Impedance, EMG, and biological torque control algorithms can all be categorized under the mid-level layer [12, 22, 31]. Of those algorithms, majority of them convert input data into trajectory or torque output for the exoskeleton. Even though torque-based algorithms are complex to implement, they are much more dynamic compared to trajectory-based algorithms. One can quickly deploy different types of torque profiles for different applications. Several exoskeletons have showed positive metabolic results using torque-based algorithms for their mid-level layer [11, 32]. Both Hip Exo v1.0 and v2.0 use torque-based algorithms for their mid-level layer.

The mid-level layer generates the appropriate torque profile based on three key parameters: onset timing, duration, and magnitude. Those three parameters often play a significant role on the overall effectiveness of a control strategy.

3.1.3 Low-level Layer

The low-level layer takes the mid-level layer's torque command and compares it against the actual torque output registered by the strain gauge. A PD feedback loop ensures the low-level layer achieves the torque demanded by the mid-level layer (Fig 12). The strain gauges measure the spring deflection and output an analog reading. The microprocessor converts the voltage reading to the ball-screw forces through the pre-calibrated regression model mentioned in the mechatronics section. The measured torque (τ_{mea}) can be calculated based on the alpha angle (α) and ball-screw force (F_{ball}). The torque error (e) is calculated by subtracting the measured torque (τ_{mea}) from desired torque (τ_{des}). The PD torque output is converted to an appropriated PWM signal through known gear reductions and motor current equations. Note that all three control strategies presented in this thesis consist of the same low-level layer for torque sensing and error compensation.

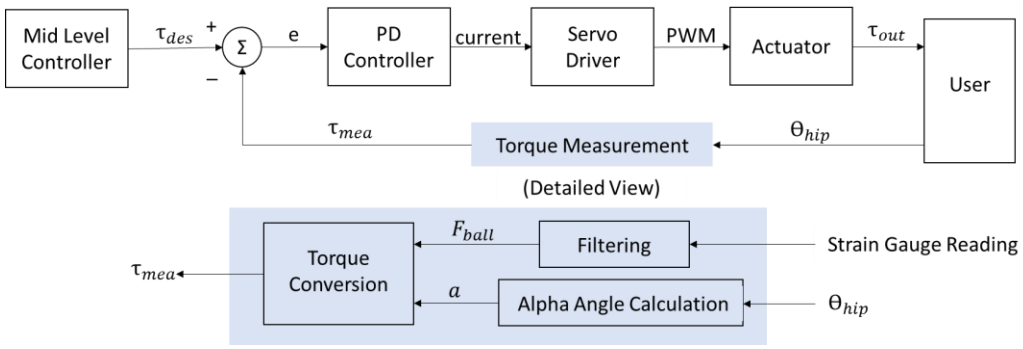

Figure 12. Low-level layer consists of a closed-loop torque controller. The PD controller ensures that the demanded torque from the mid-level layer matches the measured strain gauge output torque.

There is a special type of mode called zero-impedance mode, where the low-level input torque command is always set to zero. Due to the high gear reduction stage in the mechanical transmission, the exoskeleton exerts nonnegligible interaction torque to the user and hinders natural movements. To minimize this resistance, the device outputs an equal but opposite amount of torque to allow the user to move the limb freely, hence called zero-impedance mode. Both Hip Exo v1.0 and Hip Exo v2.0 is benchmark with able-body subjects walking at 0.4 m/s under two conditions: power-off mode and zero-impedance mode (Fig. 13). The power-off mode shows the required back-drive torque whereas the zero-impedance mode shows how the controller-compensated torque. For Hip Exo v1.0, the zero-impedance mode successfully mitigates the RMS torque error from 4.66 Nm to 0.94 Nm. However, there still exists non-negligible torques due to the device limitations. For Hip Exo v2.0, the RMS torque error is now only 0.67 Nm for power-off mode and 0.10 Nm for zero-impedance mode. In addition, for trapezoidal torque profile tracking, the Hip Exo v2.0 improved the RMSE significantly from 3.83 Nm to 1.21 Nm over a gait cycle.

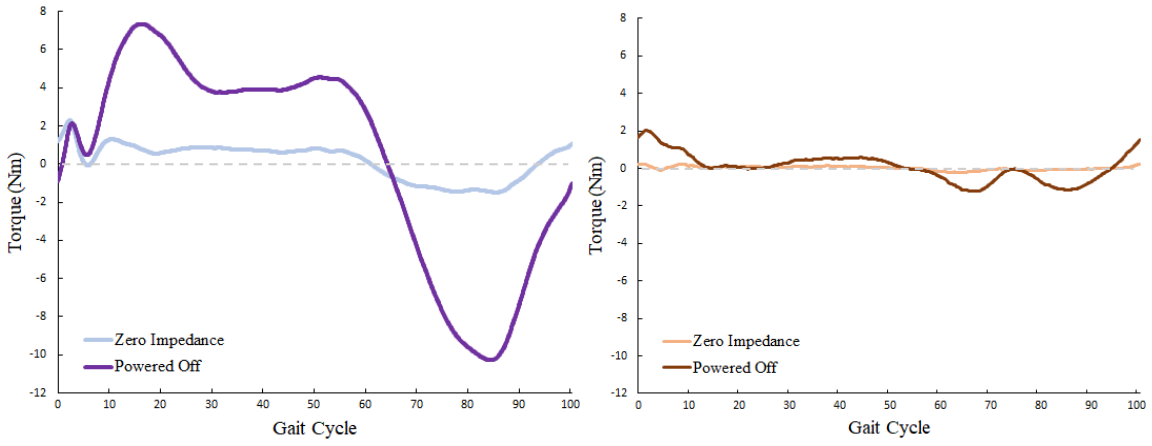

Figure 13. Hip Exo v1.0 and Hip Exo v2.0's power-off vs zero-impedance mode at 0.4 m/s. Both exoskeleton's zero-impedance mode are effective in mitigating the interaction torque. (Left) Hip Exo v1.0 (Right) Hip Exo v2.0

3.2 Biological Torque Controller

The biological torque controller mimics the human biological hip moment profile. Over a gait cycle, the controller can generate a torque assistance for both hip flexion and extension with predefined control parameters. It uses FSRs to perform high-level gait phase estimation. Then the mid-level layer generates trapezoidal torque profiles and sends the command to the low-level layer based on the current gait cycle. Three key parameters used to create the assistance profiles are: onset timing, assistance magnitude, and assistance duration (Fig. 14). The controller is not very adaptive to the user since the assistance profile does not vary once it is pre-defined.

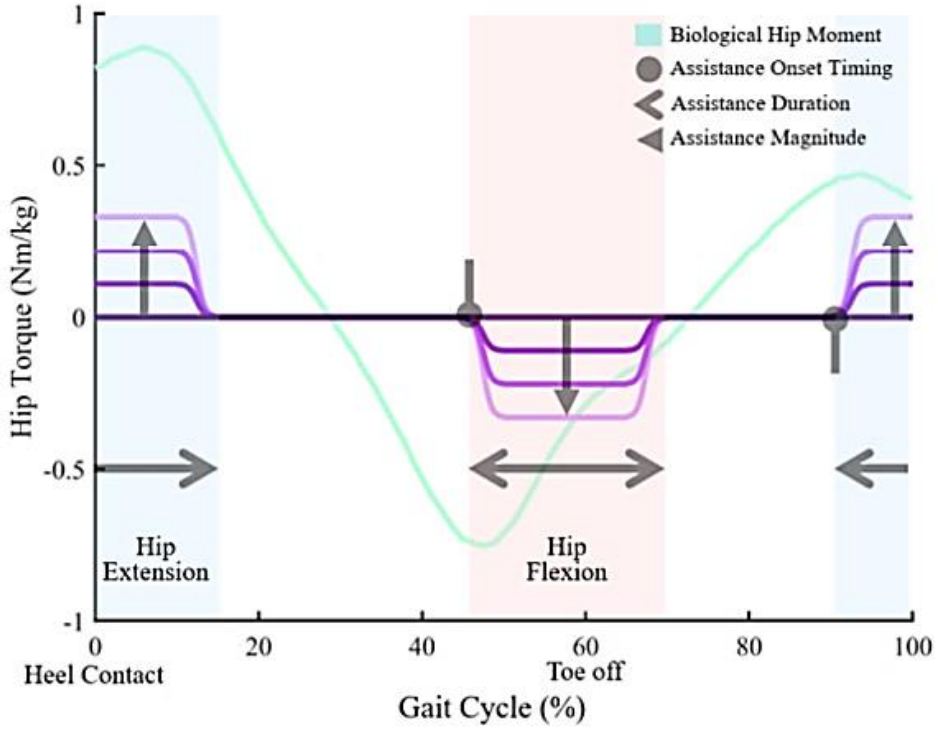

Figure 14. Example of a commanded torque profile for a biological torque controller. Control profile (shown in purple) emulates a percentage of human biological hip moment (shown in green) over a gait cycle. Hip flexion (red region) and extension (blue region) assistance onset timing, duration, and magnitude (shown with different type of arrows) can be tuned for a desired profile.

It is critical for the exoskeleton to provide assistance only at the right time, which can be represented by gait phase (Fig. 14). Hip Exo v1.0 uses a continuous regression model ranging from 0% to 100% for its gait phase estimator (where 0% is defined as the heel contact). An FSR is configured in a voltage divider setup and attached to each of the user's heel. The FSRs act as an event marker by triggering a 5V reading during heel contact. The microprocessor stores the timestamp of the heel contact. The time difference between two consecutive heel contacts is the estimated cadence. An average step time can be computed by averaging the latest 5 cadences. The time elapsed since the most recent heel strike can be interpolated as the current gait phase by dividing over the average cadence. Although the estimation algorithm is fairly robust and simple to implement, it assumes the user is walking at a constant speed with little step-to-step variation. The high-level controller will experience delay in its estimation if the user suddenly changes his/her walking speed. As a result, it can only be used in controlled walking conditions, such as constant speed treadmill walking.

Once the gait cycle estimation is received, the mid-level controller sends the torque command based on the pre-generated torque profile. The hip flexion and hip extension onset timing parameters determine when the assistance will be active. For the biological torque controller deployed, the flexion and extension timings are set to 45% and 90% of the gait cycle based on a previous hip exoskeleton study [33]. A pilot study benchmarks 15% - 30% assistance duration against metabolic performance and final assistance duration is set to 25% of the gait cycle. For the assistance magnitude study, the magnitude is the independent parameter used to investigate its metabolic impacts. Literatures have shown that human biological hip torque varies depending on speed and body-weight [34]. Thus,

the exoskeleton assistance magnitude is set to match a percentage of peak human biological hip moment. The calculation for the pre-generated torque profile is detailed in the following section.

The biological torque controller (Eq. 2) intakes a gait phase percentage, x, as an input and outputs a commanded torque, $f(x)$, where o_f and o_e are flexion and extension onset timing respectively and d is the assistance duration all relative to the gait phase.

$$f(x) = \begin{cases} -g(x - o_f), o_f \leq x \ < mod((o_f + d),100) \\ g(x - o_e), o_e \leq x \ < mod((o_e + d),100) \\ 0, otherwise \end{cases} \quad (2)$$

$g(z)$ represents a function generating a single trapezoidal profile (Eq. 3) with a desired assistance magnitude u, input phase z, assistance u starting and ending set point s_1 and s_2 respectively, all relative to the gait phase. The assistance magnitude u (Eq. 4) is computed using the desired assistance level a (%) and the peak human biological hip moment, $\tau(v)_{peak}$, calculated from Eq. 4. The biological controller is developed so that the researchers can modify all three parameters during experiments. Note that the exoskeletons are put to zero impedance mode during the no assistance part of the gait cycle.

$$g(z) = \begin{cases} \frac{uz}{s_1}, & 0 \leq z \ < s_1 \\ u, & s_1 \leq z \ < s_2 \\ -\frac{u(z - s_2)}{d - s_2} + u, & s_2 \leq z \ < d \end{cases} \quad (3)$$

$$u = \ a\tau(v)_{peak} \quad (4)$$

3.3 Proportional EMG Controller

Most of the commercial and research exoskeletons use mechanical sensors to interpret the user's intention and command the robot accordingly [4, 10, 11, 14, 23, 26]. Such a control strategy often lags behind the user's movement and has difficulty adapting to disturbances. A different type of muscle-based control strategy, the electromyography (EMG) controller, is becoming more feasible in recent years due to technological breakthroughs, especially in computational power and machine learning areas. EMG readings are highly correlated to the user's intention as they contain information about the user's muscle movements. As a result, EMG controllers can often achieve pseudo-volitional control. The inherent electromechanical delay of the EMG signals means the signals are generated about 30-100ms before muscle contractions [35]. By interpreting the EMG signals, the exoskeleton can determine the user's intention ahead of time and generate assistance in line with muscle movements. While extremely popular and well-studied in upper-limb exoskeletons, the only commercially available lower-limb exoskeleton that uses EMG as part of its control algorithm is HAL [36].

Of the various EMG-based controller, the proportional EMG controller is considered the gold standard due to its simplicity. The proposed proportional EMG controller uses the same FSR estimator for its high-level layer. The mid-level layer takes the EMG signals from relevant muscles and converts them to exoskeleton torques. Rectus femoris (RF) and gluteus maximus (GM) are two of the most accessible surface hip flexor and extensor muscles (Fig. 15). Hence, one EMG electrode is attached to RF for exoskeleton flexion command, while another is attached to GM for extension command. The torque assistance profile is created by multiplying the filtered EMG signal to a constant gain ($\times G$).

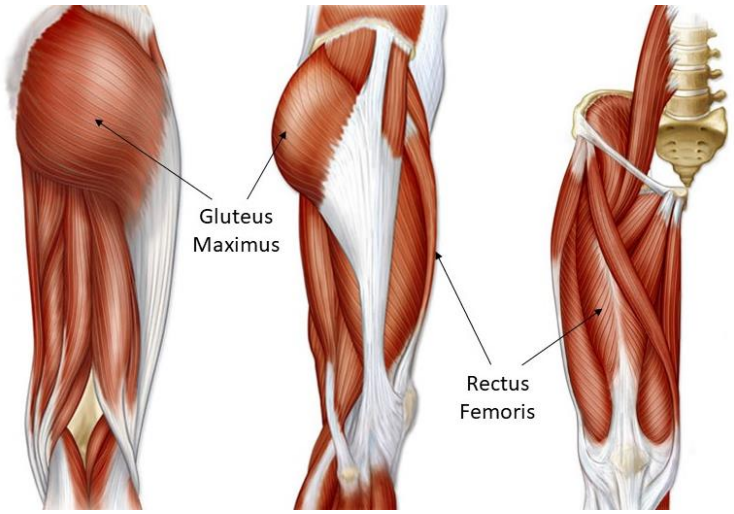

Figure 15. Main hip extension (gluteus maximus) and flexion (rectus femoris) muscles used by the proportional EMG controller.

The microprocessor samples the raw EMG signal (DataLINK, Biometrics Ltd, UK) at 1 kHz to minimize aliasing. To avoid potential phase shift, the controller uses a simple root mean square (RMS) filter with a minimal window size of 10ms (Fig. 16). To prevent misfiring due to noise, every user's EMG threshold ($V_{threshold}$) needs to be custom tuned (Eq. 5). The subject stands for a minute to collect the baseline EMG RMS reading ($V_{baseline}$) and EMG RMS standard deviation ($\sigma_{baseline}$). When the EMG reading passes a preset threshold, the commanded exoskeleton torque is scaled proportionally with the EMG reading by a gain constant ($\times G$). Note there are a total of 4 tunable thresholds.

$$V_{threshold} = V_{baseline} + 3 \times \sigma_{baseline} \tag{5}$$

Since there are two input signals (GM & RF) for each side of the exoskeleton, one of the main challenges for EMG controller is deciding which channel to use as the input throughout the gait cycle. During walking, both RF and GM can co-contract and activate at the same time. The controller needs to select the proper muscle signal because the output

torque directions are opposite (flexion vs. extension). One way to determine which muscle signal to use is through the high-level gait phase estimator. The hip is primarily extending during late swing to early stance (90% - 20%) and primarily flexing during late stance to mid swing (40% - 70%). A conservative discard state-machine is implemented where the controller disregards the hip flexor readings during 80% – 30% of the gait cycle (and vice versa for hip extensor). Therefore, only certain part of the EMG RMS signal will be converted to the exoskeleton torque profile (Fig. 16).

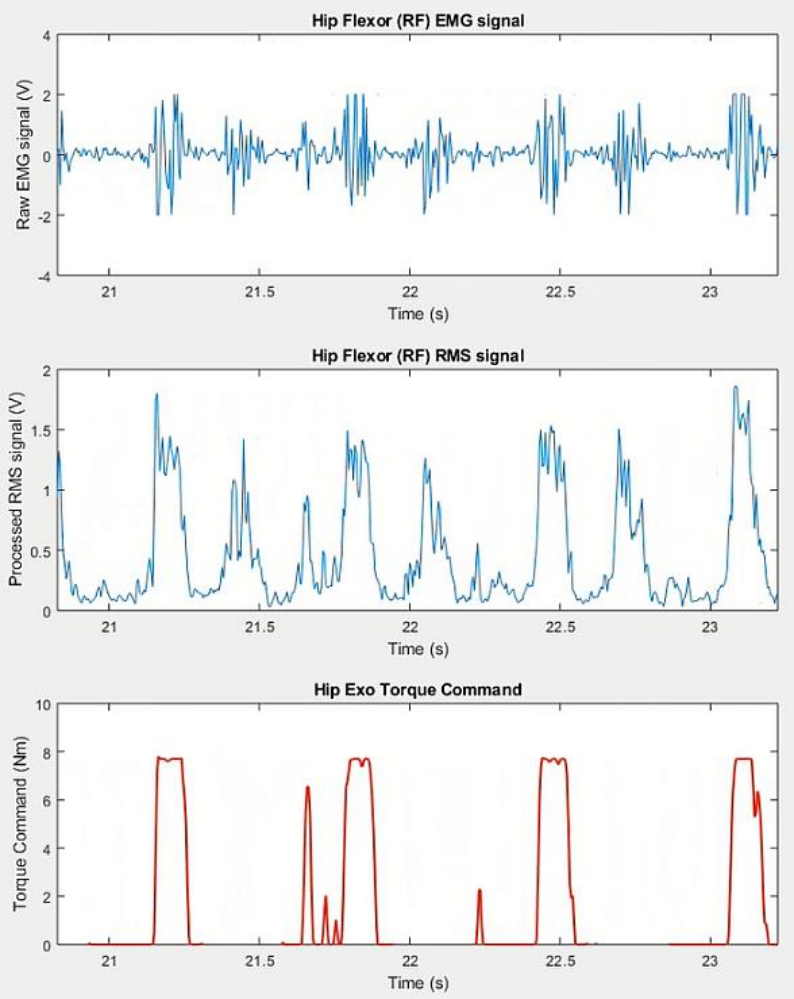

Figure 16. An example of RF's EMG signal to Hip Exo torque output. The raw RF signals are first filtered by a 10ms RMS window. Then, the mid-level layer filters out the co-contraction signals by only scaling the signals from 90% - 20% of the gait cycle.

3.4 EMG Pattern Recognition Controller

Comparing to the biological torque controller, proportional EMG controller can adapt to stride by stride variations and offer the user volitional control over the exoskeleton. However, one major challenge for the proportional EMG controller is the input signal's robustness over time. Since the entire assistance profile is based on one muscle's EMG, it is a single point failure system. Over the long period of use, electrodes tend to shift due to sweat and movement and slight displacements could result in drastic EMG signal changes [37]. To achieve a more reliable and yet volitional control strategy, a novel multi-channel EMG pattern recognition algorithm is proposed. Instead of directly scaling an EMG signal, the high-level layer takes multiple EMG readings and outputs an intent classification: hip flexion, hip extension, or zero-impedance. The mid-level layer then generates a stair wise assistance profile based on the number of a given class. The EMG pattern recognition controller can be considered as the hybrid of the two previously mentioned controllers.

The high-level layer consists of a machine learning model that determines whether the user is in hip flexion, hip extension, or zero-impedance state. A total of 16 surface EMG sensors are used, with 8 channels on each leg. Each leg's model is trained independently to ensure true leg-by-leg volitional control. Like the proportional EMG controller, the pattern recognition controller is calibrated for each individual user. To train the models, the subject wears the 16 EMG sensors and walks with the exoskeleton in zero-impedance mode (Fig. 17). The EMG sensor and motion capture data across different walking speeds are collected as training data for the model. By using reflective markers and force plates, the motion capture system (Vicon Motion Systems, UK) can reconstruct the user's lower-limb model and compute the biological hip torque through inverse dynamics. The hip

torque data is manually labelled into hip flexion, hip extension, or zero-impedance class according to % thresholds. For example, a 20% threshold means if the current torque is within ± 20% of maximal hip torque, it is labelled as a zero-impedance class. A torque value larger than +20% gets labelled as a flexion class and vice versa for the extension class. The EMG data is transformed into feature space and trained against the three hip movement classes. Once the machine learning models are trained, they are imported back to the microprocessor for real-time pattern recognition.

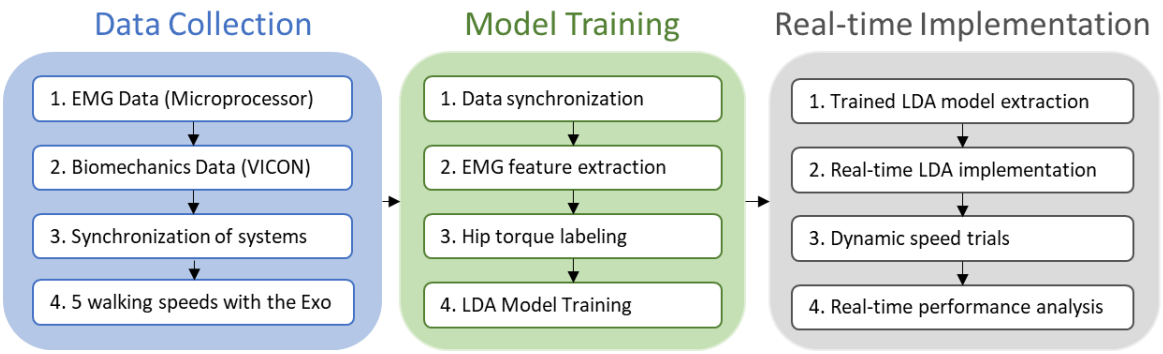

Figure 17. The EMG pattern recognition training process. The subject needs to have both the EMG sensors (inputs) and reflective markers (labels) attached and walks with the exoskeleton in zero-impedance mode. The EMG signals are synchronized and trained against the categorized labels. Finally, the relevant matrices used in the model are extracted and imported to the microprocessor. The subject walks again with the trained models to test and verify their real-time performance.

Many machine learning algorithms, such as support vector machines (SVM), neural networks (NNs), and linear discriminant analysis (LDA), have been explored for EMG pattern recognition applications by many research groups [38-41]. While SVM and NNs sometimes achieve the highest accuracy, LDA is the chosen model for its excellent accuracy and complexity trade-off. While much easier for real-time implementation, LDA only gives up minimal losses in model accuracy as seen in upper-limb studies [40, 42, 43]. A Bayes-optimal algorithm, LDA can be easily implemented on a hip exoskeleton through

a combination of state machines, statistical functions, and matrix multiplications. In short, the LDA classification is governed by the following equations (Eq. 5-6). Equation 5 is the posterior probability that an observation x is of class k. It is calculated with the density function $P(x|k)$ with mean μ_k and covariance Σ_k, the prior probability $P(k)$, and a normalization constant $P(x)$, which is the sum of k over $P(x|k)P(k)$.

$$\hat{P}(k|x) = \frac{P(x|k)P(k)}{P(x)} \tag{6}$$

$$P(x|k) = \frac{1}{(2\pi|\Sigma_k|)^{\frac{1}{2}}} \exp\left(-\frac{1}{2}(x-\mu_k)^T \Sigma_k^{-1}(x-\mu_k)\right) \tag{7}$$

In terms of hardware implementation, two 8-channel 12-Bit analog to digital convertors (MCP3208, Microchip, USA) are used to sample the 16 EMG sensors. MCP3208 is the only ADC with plastic dual in-line packages (PDIP), which allows for rapid in-house prototyping with a personal PCB mill (ProtoMat S63, LPKF, Germany). In addition, the chip uses successive approximation register (SAR) with serial peripheral interface (SPI) protocol for excellent sampling rate (100 ksps) and resolution. Due to hardware resource constraints, a dedicated off-board microprocessor with an FPGA chip (Xilinx, USA) is used to sample the EMG signals and execute the real-time pattern recognition (Fig. 18). A custom FPGA state-machine SPI driver is developed to meet the controller's demanding 16 kHz sampling rate. Each channel is stored in a 150ms buffer (150 points per channel at 1000 Hz) and the four features (MAV, ZC, SSC, WL) are extracted at 100 Hz. Then the features are multiplied through the pre-trained model's matrices and outputs the encoded hip movement class into 3 distinct analog voltage (0V,

2.5V, and 5V). The next controller update will discard the oldest 10ms data and add in the newest EMG signals to achieve the sliding window update.

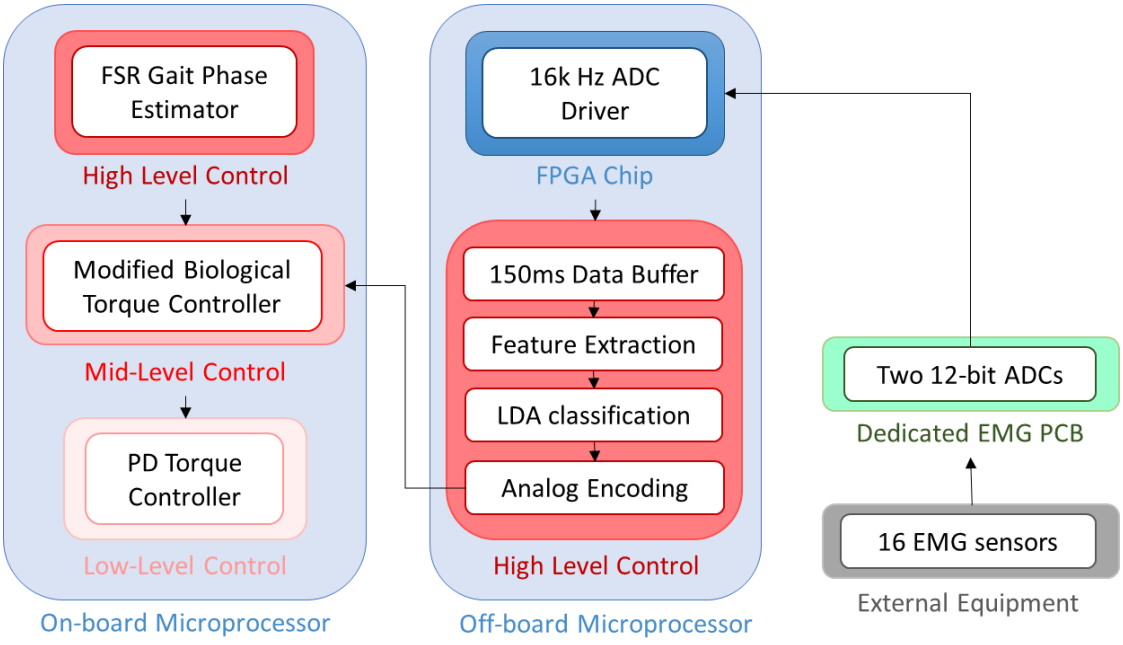

Figure 18. The extended system architecture for the EMG pattern recognition controller. An identical off-board microprocessor (NI myRIO) is used for high-level control. The FPGA chip samples two ADCs (16 EMG signals) at 16k Hz and sends the data to the high-level controller. The controller performs the pattern recognition and encodes the output classes into 3 different analog signal and sends them to the on-board mid-level controller. The on-board controller generates a stair-case like assistance profile base on the output classes from the pattern recognition controller.

A proposed on-board mid-level layer will generate stair-like torque profiles once it receives the encoded hip class from the off-board LDA model. For example, if the received class is the hip flexion, the controller would add x Nm to the current torque command (vice versa for the extension class). If the zero-impedance class is received, the torque command moves towards 0 Nm at a $0.5x$ Nm step. The assistance torque will eventually cap out at a set value or approach 0 Nm if all received classes are the same. The stair-wise ramping ensures there is not sudden torque command jumps as a result of misclassification.

CHAPTER 4. HUMAN SUBJECT TESTING AND DISCUSSION

After the exoskeletons were validated in benchtop settings, various human subject experiments were carried out to verify the exoskeletons' effectiveness. Metabolic costs, hip joint kinematics, motion captures, and EMG data were some of the matrices used for human subject evaluation. All human subject studies were approved by the Georgia Institute of Technology Institutional Review Board. Additionally, all participants were informed of the protocols and their rights before signing written consent forms.

The mid-level layer torque profile is defined through 3 parameters: onset timing, duration, and magnitude. With fixed onset timing and duration based on previous work, the biological torque controller (v1.0) was used to study the effects of varying assistance magnitude. Two versions of the proportional EMG controller were used for pilot studies: one tested the effects of assistance magnitude (v1.0) and the other on the onset timing (v2.0). The EMG pattern recognition controller (v2.0) was piloted through several offline EMG data collections. The results were used for offline modeling and optimization. Multiple verification sessions were performed to ensure microprocessor outputs matched those of the MATLAB models. An EMG sensor placement comparison also found that there was no difference between muscle-targeting and evenly-spaced configuration.

Another preliminary study showed how EMG signals contribute to high-level layer algorithms such as speed/ramp estimators. The proposed algorithms used both mechanical and EMG sensors and showed convincing accuracy improvements compared to the model based on traditional mechanical sensors only. Most importantly, 3 elderly subjects were recruited, and their data provided valuable insights into the clinical populations.

4.1 Assistance Magnitude Study (v1.0)

A biological torque controller is a simple but universal controller that only uses the onboard mechanical sensor to provide exoskeleton assistance. Previous works explored the optimal assistance duration and onset timing for the best metabolic performance [33]. This study serves as an extension to understand the metabolic impact of assistance magnitude during walking. The authors hypothesized that there is a positive correlation between the exoskeleton assistance magnitude and the metabolic reduction. The entire study was done using the biological torque controller with the Hip Exo v1.0.

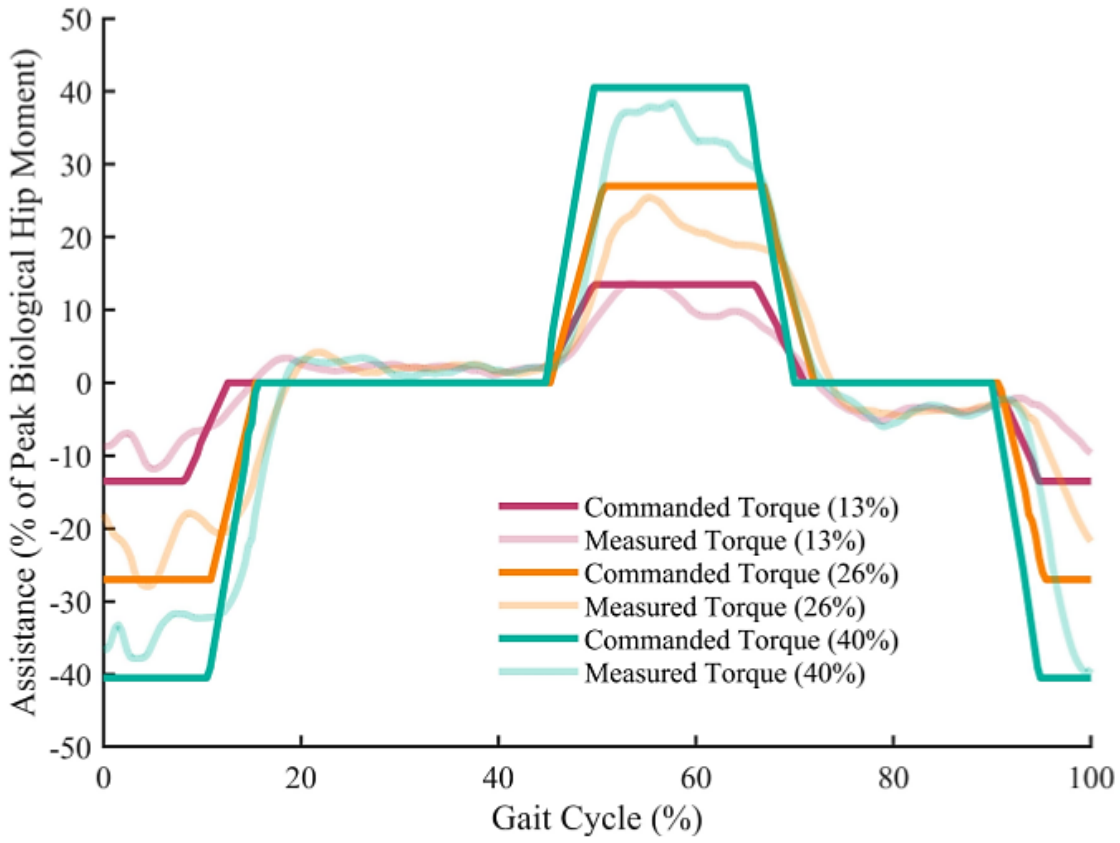

Figure 19. A torque tracking example with 3 different assistance levels (13%, 26%, and 40% of peak biological torque). Onset timing were set at 45% and 90% of the gait cycle with a duration of 25% window length. Solid lines represented the commanded torque and transparent lines represented the measured torque.

Ten healthy subjects (seven males and three females) walked on the treadmill (TuffTread, USA) at 0.8 m/s with three different assistance conditions. The assistance conditions were 13%, 26%, and 40% of the weight-normalized peak biological hip moment. An example of the three torque profiles and their respective torque tracking is shown in Fig. 19. Onset timing was set at 45% and 90% for flexion and extension assistance, and all assistance durations were set to 25% of the gait cycle. Metabolic data was collected through an indirect calorimetry system (TrueOne 2400, Parvo Medics, USA) and metabolic cost was calculated with the modified Brockway equation [44]. Hip joint torque and angle were measured through the exoskeleton's SEA and encoder sensors. An offline regression analysis across all conditions was performed to test the hypothesis.

Overall, the results demonstrated that the exoskeleton can achieve metabolic reduction with increased assistance level (Fig. 20). However, the initial hypothesis was rejected, since an increase in assistance level did not always yield a higher metabolic reduction. The resulting U-shaped trend suggested that there is an optimum point for exoskeleton assistance with respect to metabolic performance. A similar quadratic trend could be seen in an ankle exoskeleton study [18]. While the ankle and hip joints have different musculotendon structure, both studies showed that excessive assistance might penalize metabolic performances. One possible explanation of the higher metabolic cost was the irregular gait patterns observed as assistance increased. At 40% assistance, average hip kinematics were significantly biased and stride frequencies also increases increased by 12% (Fig. 20). These excessive hip flexions and increased stride frequencies manifested as a fast-paced marching gait. The rapid muscle activations might have contributed to higher metabolic consumption than the exoskeleton could help reduce [45, 46].

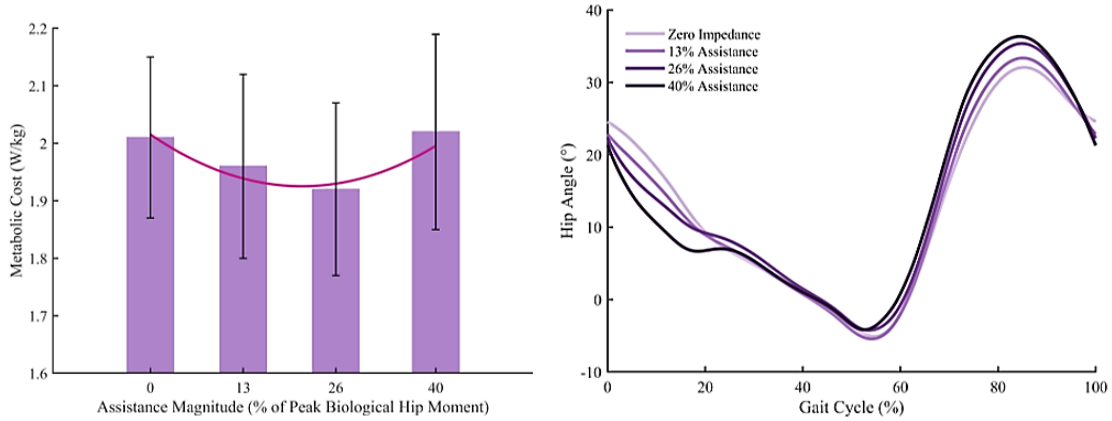

Figure 20. (Left) Metabolic cost results with different assistance magnitudes. The metabolic cost results show a U-shape trend with increased assistance magnitude. (Right) Average hip kinematics across subjects during different assistance levels. Darker shades represent higher assistance where peak hip flexion angle increases.

The overall assistance magnitude study showed a non-linear relationship between assistance magnitude and metabolic cost. While the optimal assistance magnitude generally fell in between 13% and 26%, individual data suggested that there might not be a universal optimal assistance value. Therefore, a dynamic controller such as human-in-the-loop controller or EMG-based controller might be more appropriate for achieving an individual's optimal parameters [22, 47, 48]. The findings not only provided insights into future exoskeleton designs, but also inspired several studies on EMG-based control strategies. Hip Exo v2.0 was optimized for a smaller torque range, which allowed it to outperform Hip Exo v1.0 in both benchtop testing and zero-impedance mode.

4.2 Proportional EMG Profile Pilots (v1.0)

This study aimed to create, implement, and pilot a proportional EMG controller with the Hip Exo v1.0. An external surface EMG system (DataLINK, Biometrics Ltd, UK) was used to measure the hip muscle activities. The controller proportionally scaled the signal

from a hip flexor (rectus femoris) or extensor (gluteus maximus) and outputted a torque command to the exoskeleton. The study aimed to explore the effects of proportional EMG assistance scaling with respect to both metabolic and EMG performance. The entire study was conducted using Hip Exo v1.0 with the proportional EMG controller.

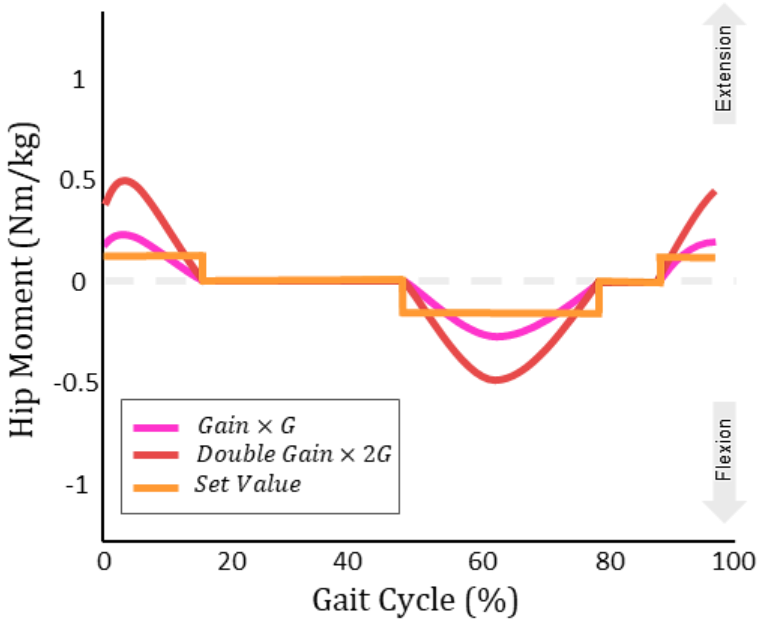

Figure 21. Three EMG-based exoskeleton assistance profiles: baseline gain (×G), double gain (×2G), and on/off set value assistance (SV). The SV condition provided a constant torque assistance with equivalent power to that of ×G condition.

One able-bodied subject walked on a treadmill at 0.8 m/s with three different EMG-based assistance profiles (Fig. 21). The first condition served as a baseline with a constant gain ($\times G$), where torque command equalled the EMG reading multiplied by the gain. The second condition had a double gain ($\times 2G$), where the torque scaled twice as fast. The third condition had an on/off set value (SV) torque command, which would only turn on when the EMG threshold was reached. The set value was defined so that the exoskeleton provided the same amount of power for both $\times G$ and SV condition, which allowed for a

direct comparison for the importance of proportional scaling. The maximum allowable torque was set to 20% of biological peak torque for safety consideration. The hip joint encoder, strain gauge, metabolic data, and EMG signals were collected for post analysis.

The EMG data was integrated over a gait cycle to numerically represent muscle activations with $\times G$ as the baseline (Fig. 22). Since muscle activation is highly correlated to muscle contraction, lower EMG values represent reduced muscle intensity. For the $\times 2G$ condition, the hip flexor (RF) had a 26.1% reduction, while the hip extensor (GM) only had a 1.8% reduction. The SV condition reduced hip flexor and extensor activity evenly by 11.5% and 11.8%. Intriguingly, the SV condition had the best metabolic reduction (8.1%), whereas the $\times 2G$ condition only had moderate amount of reduction (4.9%). The significant EMG reductions in the hip extensor muscle (GM) during 70% - 90% of the gait cycle might play a role in the better metabolic performance. However, more human subject experiments are required for further analysis.

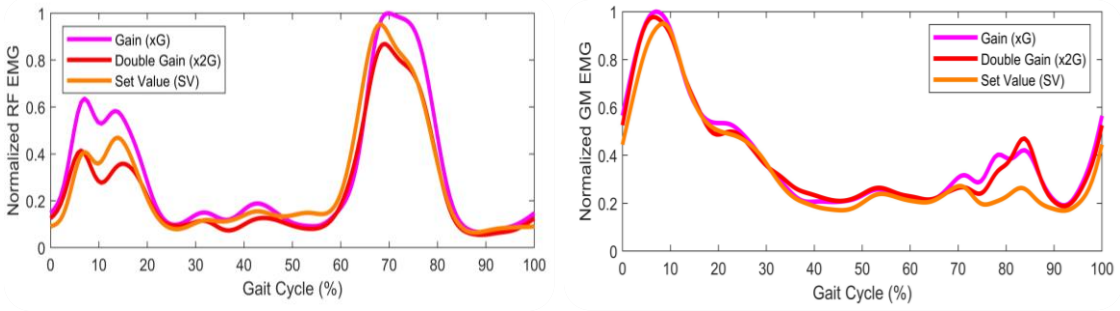

Figure 22. Normalized EMG activities over a gait cycle across all three conditions, with ×G as the baseline. (Left) Normalized hip flexor (RF) EMG signals. (Right) Normalized hip extensor (GM) EMG signals. The subject showed EMG activity reductions in both ×2G and ×SV conditions.

The purpose of this study was to design, implement, and evaluate a myoelectric controller with the Hip Exo v1.0. With simple RMS filtering, the proportional EMG

controller successfully extracted and responded to the user's intentions dynamically. The reduction in EMG activity and metabolic cost suggest that the EMG-based assistance profiles are effective. Three different EMG-based assistance profiles were investigated, and the findings suggested that the proportional scaling might not be the most important parameter for metabolic performance. Compared to the biological controller, the proportional EMG controller allowed for adaptive onset timing on a stride-by-stride basis. Two major challenges for the proportional EMG controller were controller robustness and effective threshold tuning. The controller required very precise parameter tuning for effective assistance signals and needed to be re-tuned over time to ensure signal quality. For this reason, this study inspired a different approach that utilized multiple EMG signals as the controller's inputs, which was introduced as the EMG pattern recognition controller in section 3.4.

4.3 Proportional EMG Delay Pilots (v 2.0)

The previous EMG study explored how an assistance profile might impact human subject performance. For this pilot study, the authors explored the effect of onset timing through a delayed proportional EMG controller. The controller had the same threshold tuning procedure as the one used in previous study. However, the proportional EMG assistance profile was stored in a buffer and was only commanded after a set delay had passed (Fig. 23). One able-bodied subject walked at 1.0 m/s under 6 conditions (0ms, 50ms, 100ms, 150ms, 200ms, and 300ms delay). Note that for large delay conditions (i.e. 300ms), the extension assistance was likely applied as late as early hip flexion. Therefore, the pilot study was limited to only extension assistance. Since it was an EMG-based controller, the step-by-step variation was already accounted for. Therefore, the optimal timing result for

the controller might further clarify the effect of assistance timing. Metabolic cost, assistance torque, and hip joint angle were collected with the augmented Hip Exo v2.0.

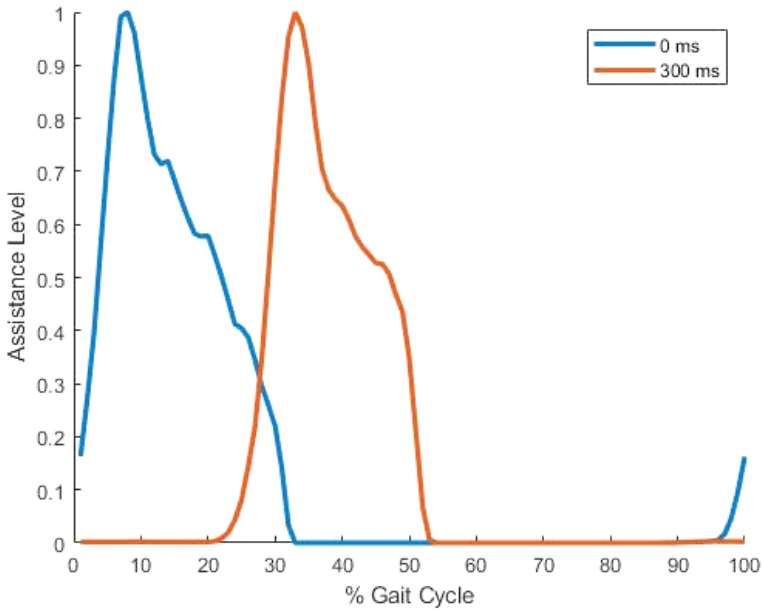

Figure 23. Examples of the delay proportional EMG controller assistances. The blue torque profile had 0ms delay whereas the orange profile had a delay of 300ms. The extension assistance was essentially applied during the early part of hip flexion.

To verify that the delayed assistance was working correctly, FSR readings were used for validation. For constant treadmill walking, the delay time could be approximated by multiplying % gait cycle shift with average cadence. For instance, the 25% assistance shift at 1 m/s would roughly translate to 300ms. The overall metabolic result showed a similar trend to that of the assistance magnitude study. An optimal metabolic performance point seemed to exist between the 0ms to 100ms delay conditions (Fig. 24). After the optimal delay point, the metabolic performance seemed to be penalized with the additional delay. The extension hip joint kinematic showed significant deviation for the 300ms condition, especially around 40% - 60% of the gait cycle (Fig. 24). The excessive extension

at the end of stand phase could have potentially contributed to the higher metabolic cost. The preliminary results agreed with the literature value of a 50 – 100ms delay between EMG signal and actual hip muscle activation [35]. Hence, this finding might give important insight into triggering exoskeleton assistance in parallel with muscle recruitments. However, additional human subject validations are required to account for the large metabolic cost variances.

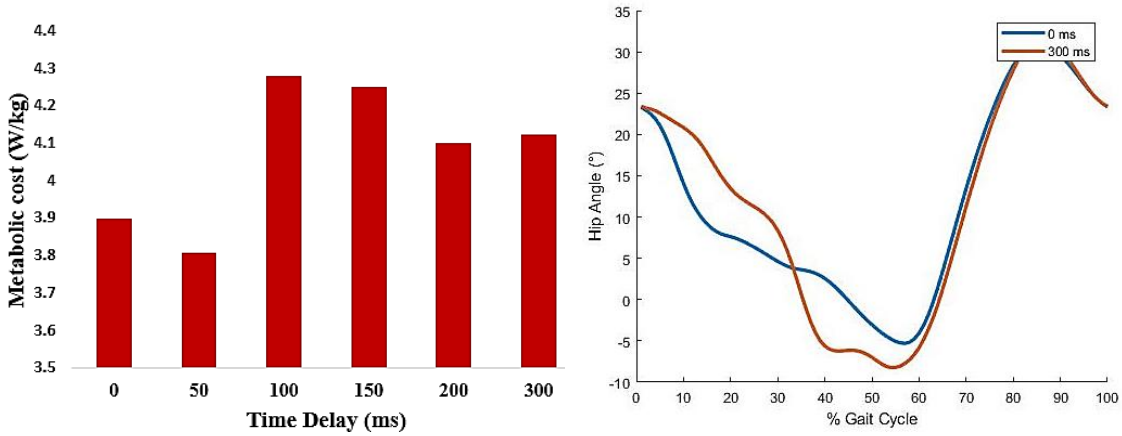

Figure 24. (Left) Metabolic cost for the different delayed EMG assistance. The optimal delay seemed to be inbetween 0ms to 100ms delay. (Right) For the 0ms condition, the EMG assistance seemed to bias the extension early on around 10% - 20% of the gait cycle.

4.4 EMG Pattern Recognition Pilots (v2.0)

While the ADC hardware and FPGA drivers were in development, three able-bodied subjects walked without the exoskeleton and their EMG and biomechanics data were collected for offline analysis. Note that all data were collected directly through the VICON system and there was no data synchronization required. All the following hyperparameters and offline models were trained with MATLAB.

For any machine learning model, hyperparameter tuning is a critical step to ensure that the model is effective and optimized. Thus, several pilot data were collected for offline analysis and optimization. There were four parameters that required tuning: EMG features, window size, sliding window, and hip torque threshold. Numerous time and frequency domain features were explored in upper-limb literatures [38, 43, 49, 50]. While time-domain features are computationally friendly on a single board computer, frequency-domain features are not due to Fourier transformations. A forward feature selection, starting with time-domain features, showed that additional frequency-domain features did not significantly improve the accuracy (Fig. 25). As a result, only four time-domain features were selected: mean absolute value (MAV), zero crossing (ZC), slope sign change (SSC), and waveform length (WL). Both ZC and SSC were selected because they provided quick estimations on the signal's frequency domain information.

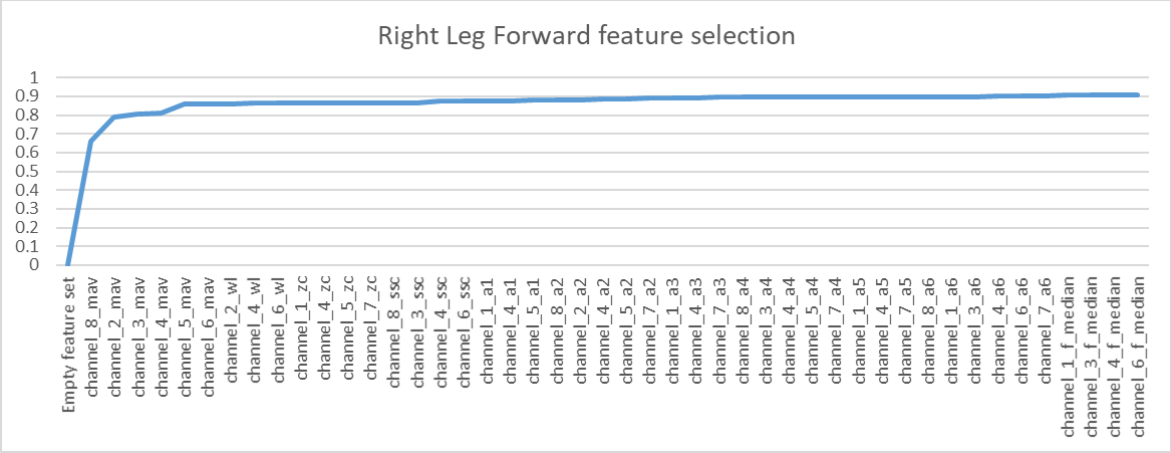

Figure 25. Forward feature selection graph for the offline data. The training accuracy already approaches the plateau even before autoregressive coefficients and frequency median features are used. Therefore, only TD features were used for development.

For real-time implementation, continuous EMG signals needed to be discretized into finite time windows and transformed into feature domains. The sliding window

determined how much new values was added before the next feature extraction. A three-dimensional parameter sweep was performed on the window size, sliding window, and hip torque threshold (Fig. 26). The sliding window difference could be seen when comparing the accuracy from top to bottom, with 150ms performed the worse and 10ms/50ms performed the same. Time windows difference could be seen when comparing every three condition to the next three, from left to right. There was little performance difference among 150ms, 200ms, and 250ms. Hence, the time window and sliding window value are selected to be 150ms and 10ms. The % threshold had significant variations because continuous hip torque was discretized into distinct classes. Since hip torque threshold were heavily subject dependent, the % values were left to be selected during real-time testing.

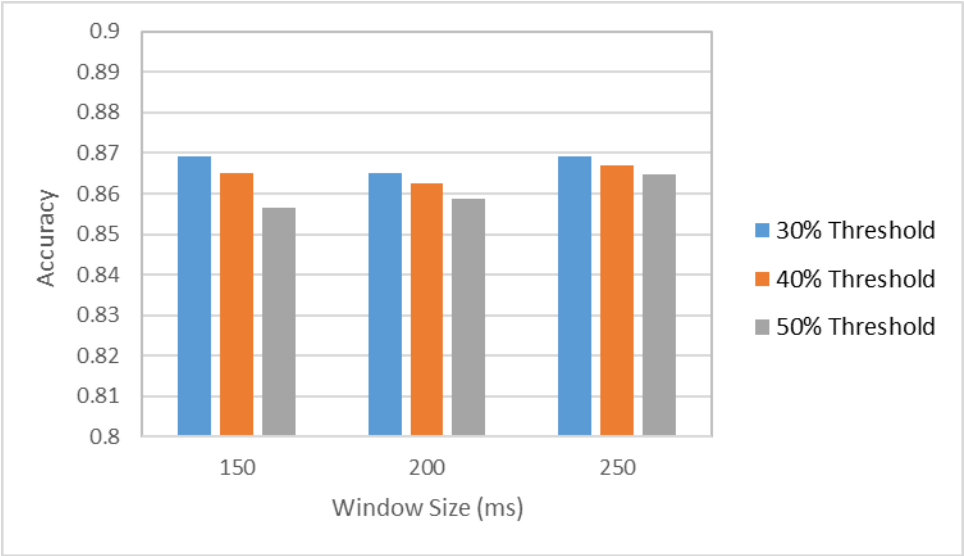

Figure 26. Time window, sliding window, and torque threshold parameter sweep for EMG Pattern recognition controller. From top to bottom, 10ms sliding windows performs the best. From left to right, all windows size performs similarly. From 15% - 50% thresholds, there are big variations in accuracies due to subject variations.

The hip torque threshold categorizes the motion capture data into the three different labels based on the % of the user's peak biological torque. While a high % threshold might

yield better accuracy due to more distinct EMG patterns, the assistance duration was often too short to be effective. In some cases, the opposite might also occur, where the assistance duration was too long for smaller thresholds (Fig. 27). As a result, a threshold parameter sweep was performed during every training and the researcher needs to decide on a case by case basis where the optimal tradeoff lied. For example, the 150ms-30% condition had an 79.03% accuracy but most of the classifications (~80%) are in flexion/extension assistance mode. However, as the threshold % increased, the model accuracy not only improved, but the flexion/extension classification also became more reasonable (~30% each). According to the pilot studies, 30% – 50% threshold was found to be most effective while achieving about 80% – 90% offline accuracy.

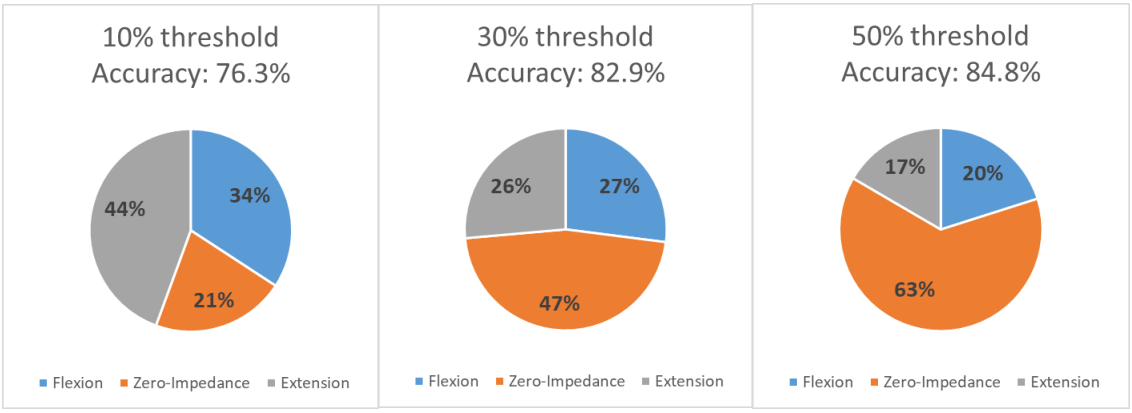

Figure 27. An example of the % class representation over one gait cycle. A healthy adult should have around 20 – 30% of hip flexion and extension during walking. While larger threshold might result in better training accuracy, the assistance duration (< 20%) may be too short to be beneficial for the user.

After the hyperparameters were set and the hardware was verified to perform as expected, five able-bodied subjects walked with Hip Exo v2.0 and their data were collected for a sensor configuration comparison. Since machine learning algorithms only look at repeated patterns in the feature space, whether the EMG sensor is targeting a specific

muscle or not should not affect its performance. To test the hypothesis, all subjects walked with two different EMG placements. For the right leg, the placement consisted of two proximal hip muscles and two rings. Each ring had three evenly spaced EMG sensors and were located at: (1) rectus femoris, (2) gluteus maximums, (3) mid vastus lateral area, (4) upper vastus medialis area, (5) mid bicep femoris area, (6) lower vastus lateral area, (7) lower vastus medialis area, and (8) lower bicep femoris area. Ch3 to Ch5 formed a 120˚ spaced upper ring in the mid-thigh region whereas Ch6 to Ch8 formed a lower ring in the lower-thigh region. For the left leg, sensors were placed directly on top of specific muscles: (9) rectus femoris, (10) gluteus maximums, (11) upper rectus femoris, (12) semitendinosus, (13) bicep femoris, (14) adductor, (15) vastus medialis, and (16) vastus lateral. In general, the two configurations performed similar with about 1% variation in accuracies and the overall average accuracy difference was 0.084%.

Many of the technical development such as dedicated PCB boards, custom FPGA driver, offline optimization, and zero-impedance simulation had pioneered the EMG pattern recognition controller. With the findings from the sensor placement comparison, it could simplify future exoskeleton designs by directly embed the thigh cuff EMG sensors in an array/ring format. This would eliminate the need for precise muscle-targeting placement such as proportional EMG controller. The next step will be to pilot EMG pattern recognition controller in real-time and evaluation the outputs against biomechanics data.

4.5 Speed & Ramp Estimator (v2.0)

Thus far, the aforementioned studies focused on using different control strategies to generate the optimal mid-level torque profile for level walking. However, to translate the exoskeleton technology outside of controlled lab environments, the high-level layer is crucial for preparing the devices for different environments. The user's state often dictates the appropriate onset timing, assistance magnitude, and duration values. In order to provide optimal assistance, the exoskeleton needs to robustly estimate the user's state through its high-level control algorithm. Two of the most important biomechanics parameters are walking speed and terrain slope. Conventional state-of-the art estimation methods often use mechanical sensors such as inertial measurement units (IMUs) [51, 52]. However, these methods are often limited by the mechanical sensor's slow update rate and signal drifts. One possible solution is to implement regressive sensor fusion models that include both mechanical and EMG sensor features [53]. As demonstrated from previous studies, EMG activities contain rich information about the user's movements such as stride-by-stride variation and acceleration/deceleration [54]. Those subtle changes in speed or ramp are often hard for mechanical sensors to capture. Therefore, the authors hypothesized that the sensor fusion estimations will be much more responsive and accurate by incorporating EMG signals. More importantly, the sensor fusion algorithm should benefit populations that have higher step-by-step variability such as elderly subjects, who were also recruited for the study. The entire study was carried out with the Hip Exo v2.0 using the zero-impedance mode and the models were trained for offline analysis. The preliminary findings will provide valuable information about speed/ramp estimation sensors for wearable robotics, which will advance the exoskeleton technology to more diverse terrains.

Four able-bodied subjects (three males and one female) and three elderly subjects (both females) were recruited for data collection. However, one elderly subject's data was excluded for the analysis due to significant sensor shifts and noise contamination. All elderly subjects were community ambulators but have much lower preferred walking speed. All subjects were asked to walk on a treadmill (Bertec Corporation, USA) with the exoskeleton in zero-impedance mode. Various static and dynamic speed/ramp data were collected. The ramp ranged from -10˚ to 10˚. The walking speed ranged from 0.8 m/s to 1.2 m/s for able-bodied subjects and 0.3 m/s to 0.7m/s for elderly subjects. Hip joint encoder, trunk IMU, and thigh IMU data were collected for mechanical sensors (6 DOF accelerometer and gyroscope data). A total of 8 channel electrodes were used for EMG data: (1) proximal rectus femoris (PRF), (2) gluteus medias (GM), (3) rectus femoris (RF), (4) biceps femoris (BF), (5) vastus medialis (VM), (6) vastus lateralis (VL), (7) adductor magnus (AM), and (8) distal biceps femoris (DBF).

For each subject, three different regressive neural network models were generated from speed and slope walking conditions using different sets of sensors: mechanical sensor data only (MECH), mechanical sensor plus 4 thigh cuff and 2 proximal region EMGs (channels 1-6) (EMG1), and mechanical sensor plus 6 thigh cuff region EMG (channels 3-8) (EMG2). Note that the 2 proximal EMG signals were from the major hip flexor (RF) and extensor (GM), which highlighted the importance of pure hip muscles (EMG1 vs. EMG2). The final features consisted of 4 mechanical features (minimum, maximum, mean, and standard deviation) and 1 EMG feature (MAV). The neural network architecture had one layer with 50 nodes and utilizes a *tanh* activation function with stochastic gradient descent. All static trials were used for training and the dynamic trial was used for testing.

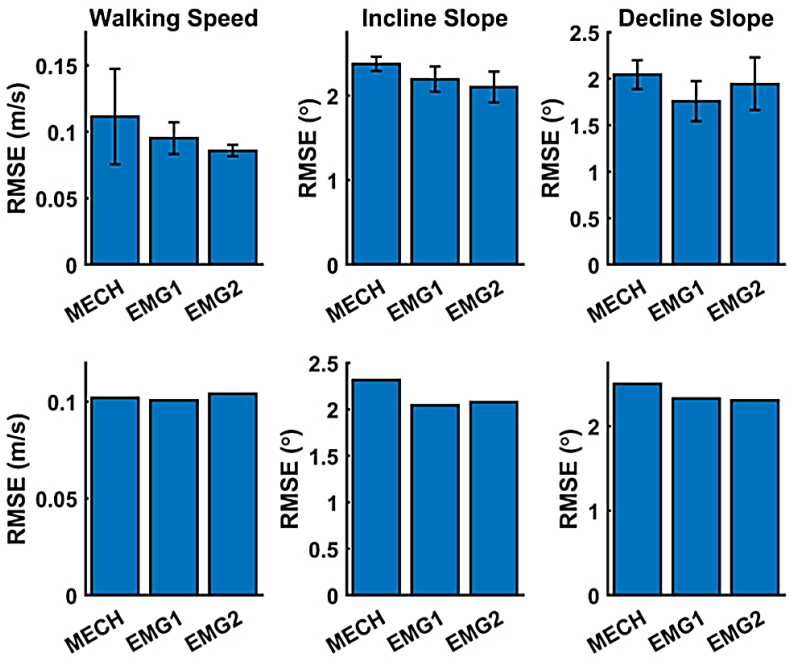

Figure 28. Dynamic trial model performance results. (Top) Able-bodied subject estimation results show that both EMG1 and EMG2 outperform the MECH in all walking conditions. (Bottom) Elderly subject estimation results show both EMG1 and EMG2 performed better than the MECH in slope estimations.

The best machine learning model achieved error rates below 0.08 m/s RMSE and 1.3˚ RMSE for speed and ramp estimation respectively (Fig. 28). Note that two separate models were used for ramp incline and decline. The study showed that additional EMG feature can significantly improve the performance. Both EMG1 and EMG2 models performed similarly, suggesting that pure hip muscles might not be critical for speed/ramp estimation. While the able-bodied results indicated consistent performance improvement (~14%) for both EMG models, the elderly subject results did not show the same trend especially for walking speed estimation. Through further EMG signal analysis, the able-bodied subjects show a positive correlation with the walking conditions whereas the elderly subjects do not. Moreover, the elderly subjects had a much smaller speed/ramp range, which might have led to insignificant EMG signal changes and thus poor performance.

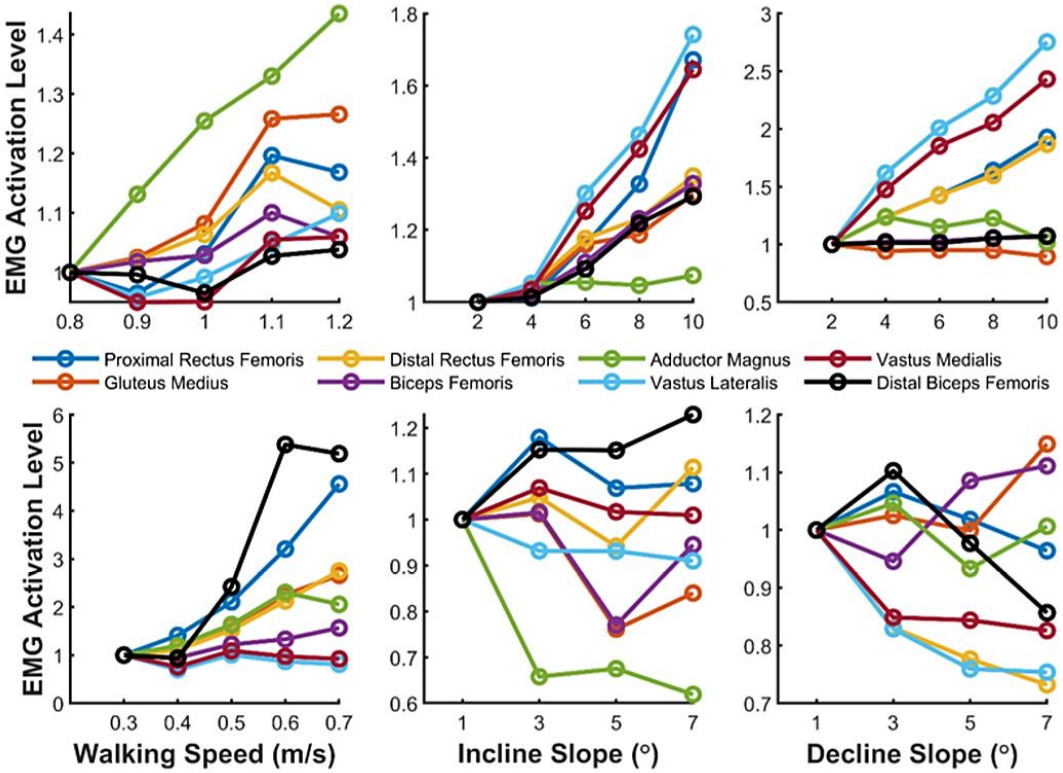

Figure 29. Average EMG activation levels across different walking speeds and slopes for able-bodied (top) and elderly (bottom) subjects. The EMG signals are represented with the maximum mean absolute value for each walking conditions.

While both populations' estimation accuracies were in similar orders of magnitude, the elderly subjects exhibited larger EMG variations (Fig. 29). The non-linear correlation may have limited the machine learning model's ability to differentiate the various conditions. The preliminary data also suggests that elderly subjects have completely different muscle recruitment strategies. For example, during decline slope walking, able-bodied subjects tended to focus on power absorption to dissipate their COM energy in the downward direction [55]. However, elderly subjects seemed to reduce their distal knee extensor activations and relied more heavily on proximal hip extensors to maintain stability. Hence, the neural network models performed differently between able-body and elderly populations.

One main reason that the both EMG models outperformed the MECH model during dynamic trials was due to trial speed and slope trajectory having an accel/deceleration section. While mechanical sensors provide sufficient information to solve a regression problem during steady state walking, they have a limitation of not being versatile in understanding the user's intention. The addition of EMG signal information plays a critical role in predicting the user's intention to either accelerate or decelerate. The capability of EMG data for user intent has already shown positive results in the literature for classifying locomotion mode transitions [56, 57]. The role of EMG becomes greater in speed and slope estimation as regression is a continuous estimation of user intent when dynamically changing the underlying walking states.

Conclusively, the proposed machine learning models can estimate the users walking speeds and slopes accurately. The study demonstrates the importance of EMG signals in high-level control layer such as slope and speed estimations. While able-bodied subjects' models improved in all trials with the additional EMG features, elderly subjects' models had more variations. Regardless of the speed/ramp model, EMG1 and EMG2 configurations showed similar results. These findings could simplify the future exoskeleton designs by integrating the EMG sensors directly into the thigh cuffs. Finally, the main limitation of this study is that all analyses were performed offline. Future studies should include additional real-time implementation of the models and more elderly subjects for statistical significance.

CHAPTER 5. CONCLUSION AND FUTURE WORK

Both Hip Exo v1.0 and v2.0 are rigid powered exoskeletons that can provide mechanical power in the hip flexion and extension directions. The clever use of elastic springs allows the devices to achieve high-fidelity closed-loop torque control. The implementations and experimentations of 3 distinct control strategies, the biological torque controller, proportional EMG controller, and EMG pattern recognition controller, highlight the benefits and shortcomings of using each controller. These controllers are fundamentally different in the type of sensors (mechanical or EMG) used to define the mid-level layer assistance torque profile. The main differences arise in the optimization of parameters and the versatility of the controller. While the biological torque controller is easy to implement, it lacks the adaptivity that the EMG controllers have. Three important parameters, onset timing, magnitude, and duration, are observed and tested to see how to each control strategy's parameter(s) impacts human subject performance, such as metabolic cost, biomechanics, and EMG activations. The exoskeletons serve as excellent test-beds for numerous research questions on understanding human-machine interactions.

The Hip Exo v1.0 was first developed to match the values reported in previous biomechanics literatures. However, the human user is an incredibly complex and dynamic set of input signals for the exoskeleton. Through the assistance magnitude and proportional EMG scaling studies, many design flaws and interaction issues of Hip Exo v1.0 became apparent. Based on the findings of those studies, an improved Hip Exo v2.0 was developed. With faster and more accurate torque response, Hip Exo v2.0 enabled several new experiments such as proportional EMG delay study and novel EMG pattern recognition

controller development. Custom FPGA drivers were development and the machine learning algorithms are implemented in Hip Exo v2.0 to help the author explore the future of intelligent autonomous exoskeletons.

For biological torque experiments, with fixed onset timing and duration, there exists an optimal magnitude for the best metabolic performance that varies between users. The EMG profile pilot showed similar results to the biological torque controller, where an optimal assistance scaling exists for the best metabolic performance. For the timing pilot, the magnitude and duration are fixed, and there seems to also be an optimal delay for best metabolic performance. Based on those pilot tests, a hypothesis was formed that a more dynamic onset timing according to EMG signal is needed, but the profile might not need to be scaled proportionally. This hypothesis leads to the creation and experimentation of the EMG pattern recognition controller. The offline results show feasibility for the next-generation intelligent controller. With the knowledge gained from the previous results, other intelligent high-level estimators are pioneered with the combination of EMG signals and mechanical sensors. The estimators utilize the both mechanical and EMG sensor information to approximate the user's walking speed and ramp angle. It is intended to push the Hip Exo v2.0 into becoming a truly autonomous platform. Many of the technical developments and human subject findings serve as clinical verdicts to guide the research direction for future powered hip exoskeletons.

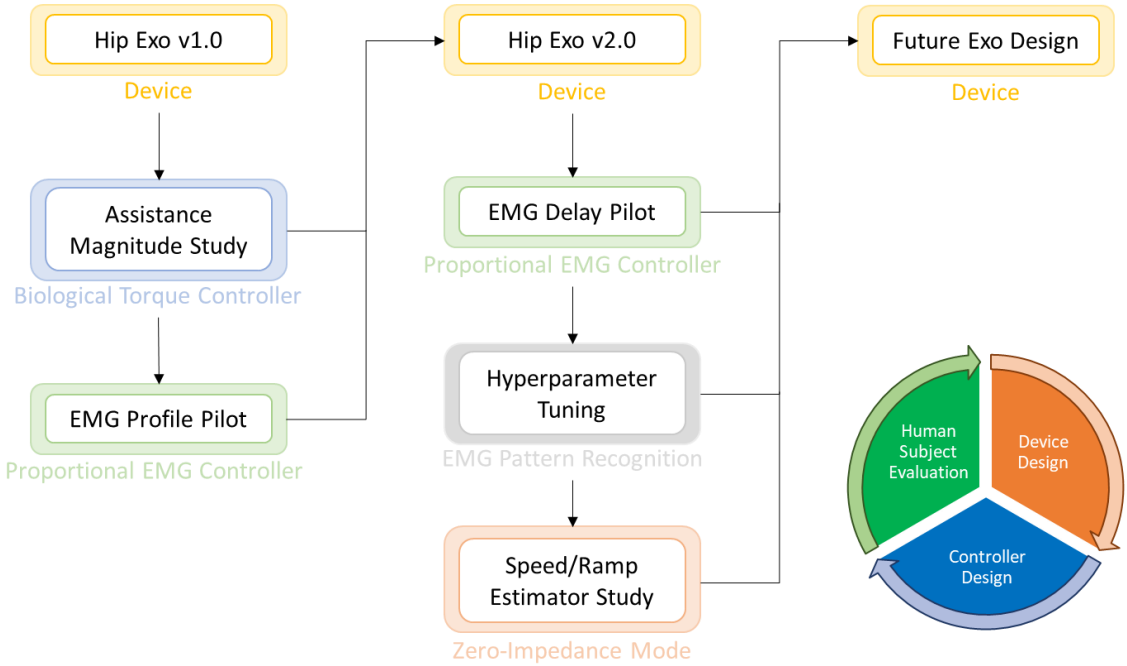

Figure 30. Summary of the Hip Exo v1.0 and v2.0's Design cycles. The device and controller allow for certain studies to be carried out. The findings of the studies are then used for the next-generation of device development.

In summary, this thesis provides three core contributions to the field of assistive lower limb robotics (Fig. 30). Firstly, it presents two versions of novel hip exoskeleton designs utilizing a ball screw driven series elastic actuator for power assistance at the hip joint. Numerous mechanical and electrical design considerations and findings are presented to help advance future wearable robot designs. Secondly, three different intelligent controllers were developed and validated in both benchtops testing and human subject testing environments. The inherent difference among the controllers allows for direct controller comparisons, which can provide valuable insight as to how the human body interacts with assistive wearables. Lastly, several human subject studies are carried out with the exoskeletons. Many of the findings serve as clinical verdicts to guide the research direction for powered hip exoskeletons.

APPENDIX A. DETAILED BALL-SCREW CALCULATIONS

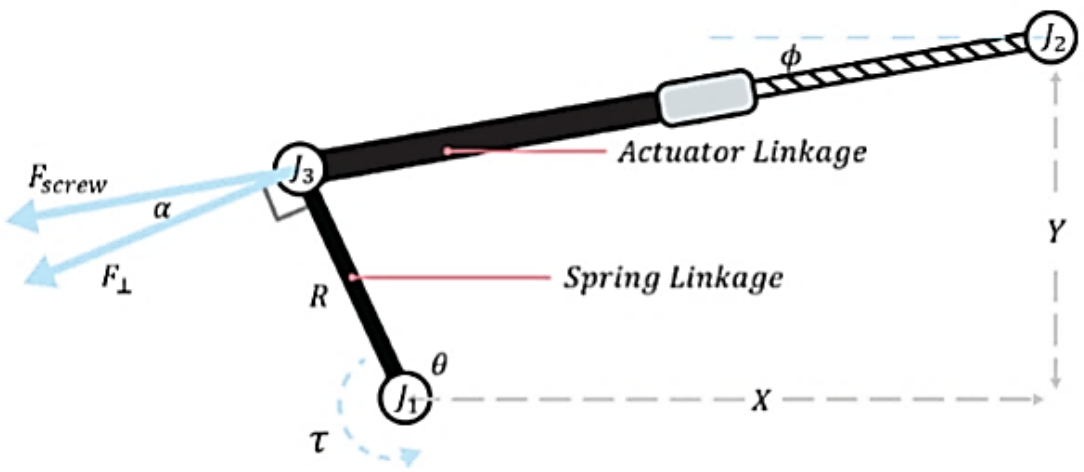

Figure 31. Torque calculation of the ball screw actuator. Blue arrow shows the ball screw actuator travel direction. Ball screw orientation angle, α, is used to convert the force exerted by the actuator to the output torque at the hip joint.

Torque conversion using the ball screw transmission is critical as it governs the desired torque input at the hip joint. The actuator rotates about two joints, J_1 and J_2 where J_1 is the output joint and J_2 is the passive joint that the actuator rotates about as ball screw actuator lengthens (Fig. 31). As there is an additional linear motion in the transmission system while translating the motor torque to the output joint torque, it is required to calculate the ball screw orientation angle, α, that will be used in converting the linear force to the output torque.

In order to calculate α, two angles θ and ϕ are required where θ is the spring linkage angle and ϕ is the ball screw linkage angle both with respect to the horizontal plane. θ can be measured directly using the absolute encoder while ϕ can be estimated using θ, moment arm length, R, and fixed horizontal and vertical distance between J_1 and J_2 noted as X and Y respectively. Using a basic trigonometry function, horizontal and vertical distance of the

actuator tip joint, J_3, can be calculated which can be used to compute ϕ. Complete equation to calculate actuator orientation angle, α, is shown by Eq. 8.

$$\alpha = \frac{\pi}{2} - (\theta + \tan^{-1}(\frac{X + R\cos\theta}{Y - R\sin\theta})) \tag{8}$$

After calculating α, the linear force exerted from the ball screw, F_{screw}, can be converted to the force perpendicular to the spring linkage, $F_{\perp}$. By using $F_{\perp}$ multiplied by the moment arm length, R, torque at the output shaft can be calculated for the entire hip joint angle range. The overall equation for converting the input motor torque to output joint torque is shown by Eq. 2, where N is the initial gear ratio of the timing belt pulley, P is the screw lead length, and τ_m is the input motor torque.

$$\tau_{hip} = \frac{2\pi NR\cos\alpha}{P}\tau_m \tag{2}$$

REFERENCES

[1] N. Yagin, "Apparatus for Facilitating Walking," Patent 440684, Nov 18, 1890.

[2] A. J. Young and D. P. Ferris, "State of the Art and Future Directions for Lower Limb Robotic Exoskeletons," (in English), *Ieee Transactions on Neural Systems and Rehabilitation Engineering,* vol. 25, no. 2, pp. 171-182, Feb 2017.

[3] S. D. Mair, A. V. Seaber, R. R. Glisson, and W. E. Garrett, Jr., "The role of fatigue in susceptibility to acute muscle strain injury," *Am J Sports Med,* vol. 24, no. 2, pp. 137-43, Mar-Apr 1996.

[4] A. B. Zoss, H. Kazerooni, and A. Chu, "Biomechanical design of the Berkeley lower extremity exoskeleton (BLEEX)," (in English), *Ieee-Asme Transactions on Mechatronics,* vol. 11, no. 2, pp. 128-138, Apr 2006.

[5] A. Esquenazi, M. Talaty, A. Packel, and M. Saulino, "The ReWalk powered exoskeleton to restore ambulatory function to individuals with thoracic-level motor-complete spinal cord injury," *Am J Phys Med Rehabil,* vol. 91, no. 11, pp. 911-21, Nov 2012.

[6] R. J. Farris, H. A. Quintero, S. A. Murray, K. H. Ha, C. Hartigan, and M. Goldfarb, "A preliminary assessment of legged mobility provided by a lower limb exoskeleton for persons with paraplegia," *IEEE Trans Neural Syst Rehabil Eng,* vol. 22, no. 3, pp. 482-90, May 2014.

[7] G. Zeilig, H. Weingarden, M. Zwecker, I. Dudkiewicz, A. Bloch, and A. Esquenazi, "Safety and tolerance of the ReWalk exoskeleton suit for ambulation by people with complete spinal cord injury: a pilot study," (in eng), *J Spinal Cord Med,* vol. 35, no. 2, pp. 96-101, Mar 2012.

[8] C. Bach Baunsgaard *et al.*, "Gait training after spinal cord injury: safety, feasibility and gait function following 8 weeks of training with the exoskeletons from Ekso Bionics," *Spinal Cord,* vol. 56, no. 2, pp. 106-116, Feb 2018.

[9] L. E. Miller, A. K. Zimmermann, and W. G. Herbert, "Clinical effectiveness and safety of powered exoskeleton-assisted walking in patients with spinal cord injury: systematic review with meta-analysis," (in eng), *Med Devices (Auckl),* vol. 9, pp. 455-66, 2016.

[10] A. T. Asbeck, S. M. M. De Rossi, K. G. Holt, and C. J. Walsh, "A biologically inspired soft exosuit for walking assistance," *The International Journal of Robotics Research,* vol. 34, no. 6, pp. 744-762, 2015.

[11] F. Giovacchini *et al.*, "A light-weight active orthosis for hip movement assistance," *Robotics and Autonomous Systems*, vol. 73, pp. 123-134, 2015/11/01/ 2015.

[12] L. M. Mooney, E. J. Rouse, and H. M. Herr, "Autonomous exoskeleton reduces metabolic cost of human walking during load carriage," *J Neuroeng Rehabil*, vol. 11, p. 80, May 9 2014.

[13] K. Seo, J. Lee, Y. Lee, T. Ha, and Y. Shim, "Fully autonomous hip exoskeleton saves metabolic cost of walking," in *2016 IEEE International Conference on Robotics and Automation (ICRA)*, 2016, pp. 4628-4635.

[14] K. Witte, J. Zhang, R. W. Jackson, and S. H. Collins, *Design of Two Lightweight, HighBandwidth Torque-Controlled Ankle Exoskeletons*. 2015.

[15] G. J. Androwis, K. Karunakaran, E. Nunez, P. Michael, G. Yue, and R. A. Foulds, "Research and development of new generation robotic exoskeleton for over ground walking in individuals with mobility disorders (Novel design and control)," in *2017 International Symposium on Wearable Robotics and Rehabilitation (WeRob)*, 2017, pp. 1-2.

[16] K. A. Strausser, T. A. Swift, A. B. Zoss, H. Kazerooni, and B. Bennett, *Mobile Exoskeleton for Spinal Cord Injury: Development and Testing*. 2011.

[17] Y. Kusuda, "In quest of mobility – Honda to develop walking assist devices," *Industrial Robot: the international journal of robotics research and application*, vol. 36, no. 6, pp. 537-539, 2009.

[18] S. H. Collins, M. B. Wiggin, and G. S. Sawicki, "Reducing the energy cost of human walking using an unpowered exoskeleton," *Nature*, vol. 522, p. 212, 04/01/online 2015.

[19] G. S. Sawicki, C. L. Lewis, and D. P. Ferris, "It pays to have a spring in your step," *Exercise and sport sciences reviews*, vol. 37, no. 3, p. 130, 2009.

[20] L. Grazi, S. Crea, A. Parri, R. Molino Lova, S. Micera, and N. Vitiello, "Gastrocnemius Myoelectric Control of a Robotic Hip Exoskeleton Can Reduce the User's Lower-Limb Muscle Activities at Push Off," (in English), *Frontiers in Neuroscience*, Original Research vol. 12, no. 71, 2018-February-14 2018.

[21] I. Kang, H. Hsu, and A. Young, "The Effect of Hip Assistance Levels on Human Energetic Cost Using Robotic Hip Exoskeletons," *IEEE Robotics and Automation Letters*, vol. 4, no. 2, pp. 430-437, 2019.

[22] A. J. Young, H. Gannon, and D. P. Ferris, "A Biomechanical Comparison of Proportional Electromyography Control to Biological Torque Control Using a Powered Hip Exoskeleton," *Frontiers in Bioengineering and Biotechnology*, vol. 5, p. 37, 2017.

[23] M. K. Shepherd and E. J. Rouse, "Design and Validation of a Torque-Controllable Knee Exoskeleton for Sit-to-Stand Assistance," *IEEE/ASME Transactions on Mechatronics,* vol. 22, no. 4, pp. 1695-1704, 2017.

[24] J. J. Eng and D. A. Winter, "Kinetic analysis of the lower limbs during walking: What information can be gained from a three-dimensional model?," *Journal of Biomechanics,* vol. 28, no. 6, pp. 753-758, 1995/06/01/ 1995.

[25] N. Paine, S. Oh, and L. Sentis, "Design and Control Considerations for High-Performance Series Elastic Actuators," *IEEE/ASME Transactions on Mechatronics,* vol. 19, no. 3, pp. 1080-1091, 2014.

[26] T. Zhang, M. Tran, and H. Huang, "Design and Experimental Verification of Hip Exoskeleton With Balance Capacities for Walking Assistance," *IEEE/ASME Transactions on Mechatronics,* vol. 23, no. 1, pp. 274-285, 2018.

[27] N. Instruments, "Measuring Strain with Strain Gages," Mar 19 2019.

[28] J. E. Bertram and A. Ruina, "Multiple walking speed-frequency relations are predicted by constrained optimization," *J Theor Biol,* vol. 209, no. 4, pp. 445-53, Apr 21 2001.

[29] A. J. Young, A. M. Simon, N. P. Fey, and L. J. Hargrove, "Intent recognition in a powered lower limb prosthesis using time history information," (in eng), *Annals of biomedical engineering,* vol. 42, no. 3, pp. 631-641, 2014/03// 2014.

[30] H. A. Quintero, R. J. Farris, and M. Goldfarb, "A Method for the Autonomous Control of Lower Limb Exo-skeletons for Persons with Paraplegia," (in eng), *Journal of medical devices,* vol. 6, no. 4, pp. 0410031-0410036, 2012.

[31] J. A. Blaya and H. Herr, "Adaptive control of a variable-impedance ankle-foot orthosis to assist drop-foot gait," *IEEE Transactions on Neural Systems and Rehabilitation Engineering,* vol. 12, no. 1, pp. 24-31, 2004.

[32] B. T. Quinlivan *et al.*, "Assistance magnitude versus metabolic cost reductions for a tethered multiarticular soft exosuit," *Science Robotics,* vol. 2, no. 2, p. eaah4416, 2017.

[33] A. J. Young, J. Foss, H. Gannon, and D. P. Ferris, "Influence of Power Delivery Timing on the Energetics and Biomechanics of Humans Wearing a Hip Exoskeleton," (in eng), *Frontiers in bioengineering and biotechnology,* vol. 5, pp. 4-4, 2017.

[34] K. E. Zelik and A. D. Kuo, "Human walking isn't all hard work: evidence of soft tissue contributions to energy dissipation and return," (in eng), *The Journal of experimental biology,* vol. 213, no. Pt 24, pp. 4257-4264, 2010.

[35] H. Begovic, G.-Q. Zhou, T. Li, Y. Wang, and Y.-P. Zheng, "Detection of the electromechanical delay and its components during voluntary isometric contraction of the quadriceps femoris muscle," (in eng), *Frontiers in physiology*, vol. 5, pp. 494-494, 2014.

[36] H. Kawamoto, L. Suwoong, S. Kanbe, and Y. Sankai, "Power assist method for HAL-3 using EMG-based feedback controller," in *Systems, Man and Cybernetics, 2003. IEEE International Conference on*, 2003, vol. 2, pp. 1648-1653 vol.2.

[37] L. Hargrove, K. Englehart, and B. Hudgins, "The effect of electrode displacements on pattern recognition based myoelectric control," in *2006 International Conference of the IEEE Engineering in Medicine and Biology Society*, 2006, pp. 2203-2206.

[38] M. Asghari Oskoei and H. Hu, "Myoelectric control systems—A survey," *Biomedical Signal Processing and Control*, vol. 2, no. 4, pp. 275-294, 2007/10/01/ 2007.

[39] B. Hudgins, P. Parker, and R. N. Scott, "A new strategy for multifunction myoelectric control," *IEEE Transactions on Biomedical Engineering*, vol. 40, no. 1, pp. 82-94, 1993.

[40] N. Nazmi, M. A. Abdul Rahman, S.-I. Yamamoto, S. A. Ahmad, H. Zamzuri, and S. A. Mazlan, "A Review of Classification Techniques of EMG Signals during Isotonic and Isometric Contractions," (in eng), *Sensors (Basel, Switzerland)*, vol. 16, no. 8, p. 1304, 2016.

[41] E. Scheme and K. Englehart, *Electromyogram pattern recognition for control of powered upper-limb prostheses: State of the art and challenges for clinical use*. 2011, pp. 643-59.

[42] K. Englehart and B. Hudgins, "A robust, real-time control scheme for multifunction myoelectric control," *IEEE Transactions on Biomedical Engineering*, vol. 50, no. 7, pp. 848-854, 2003.

[43] X. xi, M. Tang, S. M. Miran, and Z. Luo, *Evaluation of Feature Extraction and Recognition for Activity Monitoring and Fall Detection Based on Wearable sEMG Sensors*. 2017, p. 1229.

[44] J. M Brockway, *Derivation of formulae used to calculate energy expenditure in man*. 1987, pp. 463-71.

[45] A. D. Kuo, *A Simple Model of Bipedal Walking Predicts the Preferred Speed–Step Length Relationship*. 2001, pp. 264-9.

[46] J. Doke, J. M. Donelan, and A. D. Kuo, "Mechanics and energetics of swinging the human leg," *The Journal of Experimental Biology*, vol. 208, no. 3, p. 439, 2005.

[47] Y. Ding, M. Kim, S. Kuindersma, and C. J. Walsh, "Human-in-the-loop optimization of hip assistance with a soft exosuit during walking," *Science Robotics,* vol. 3, no. 15, p. eaar5438, 2018.

[48] J. Zhang *et al.*, "Human-in-the-loop optimization of exoskeleton assistance during walking," *Science,* vol. 356, no. 6344, p. 1280, 2017.

[49] A. Phinyomark, C. Limsakul, and P. Phukpattaranont, *A Novel Feature Extraction for Robust EMG Pattern Recognition*. 2009, pp. 71-80.

[50] E. Scheme and K. Englehart, "On the robustness of EMG features for pattern recognition based myoelectric control: a multi-dataset comparison," (in eng), *Conf Proc IEEE Eng Med Biol Soc,* vol. 2014, pp. 650-3, 2014.

[51] Q. Li, M. Young, V. Naing, and J. M. Donelan, "Walking speed and slope estimation using shank-mounted inertial measurement units," in *2009 IEEE International Conference on Rehabilitation Robotics*, 2009, pp. 839-844.

[52] Q. Li, M. Young, V. Naing, and J. M. Donelan, "Walking speed estimation using a shank-mounted inertial measurement unit," *Journal of Biomechanics,* vol. 43, no. 8, pp. 1640-1643, 2010/05/28/ 2010.

[53] A. Young, T. A. Kuiken, and L. Hargrove, *Analysis of using EMG and mechanical sensors to enhance intent recognition in powered lower limb prostheses*. 2014, p. 056021.

[54] A. Erdemir, S. McLean, W. Herzog, and A. J. van den Bogert, "Model-based estimation of muscle forces exerted during movements," *Clinical Biomechanics,* vol. 22, no. 2, pp. 131-154, 2007/02/01/ 2007.

[55] J. R. Montgomery and A. M. Grabowski, "The contributions of ankle, knee and hip joint work to individual leg work change during uphill and downhill walking over a range of speeds," *R Soc Open Sci,* vol. 5, no. 8, p. 180550, Aug 2018.

[56] A. J. Young and L. J. Hargrove, "A Classification Method for User-Independent Intent Recognition for Transfemoral Amputees Using Powered Lower Limb Prostheses," *IEEE Transactions on Neural Systems and Rehabilitation Engineering,* vol. 24, no. 2, pp. 217-225, 2016.

[57] H. Huang, F. Zhang, L. J. Hargrove, Z. Dou, D. R. Rogers, and K. B. Englehart, "Continuous Locomotion-Mode Identification for Prosthetic Legs Based on Neuromuscular–Mechanical Fusion," *IEEE Transactions on Biomedical Engineering,* vol. 58, no. 10, pp. 2867-2875, 2011.